Received: 5 October 2024 | Revised: 7 May 2025 | Accepted: 13 May 2025

DOI: 10.1002/qj.5024

Quarterly Journal of the Royal Meteorological Society RMetS

RESEARCH ARTICLE

The role of thermal stratification on the co-spectral properties of momentum transport above an Amazonian forest

Luca Mortarini[1] | **Gabriel Katul**[2] | **Ivan Mauricio Cely-Toro**[3] | **Cléo Quaresma Dias-Júnior**[4] | **Ivan Mammarella**[5]

[1]Università di Milano, Dipartimento di Scienze della Terra 'Ardito Desio', Milan, Italy

[2]Department of Civil and Environmental Engineering, Duke University, Durham, North Carolina

[3]Air Resources Laboratory, National Oceanic and Atmospheric Administration (NOAA), Oak Ridge, Tennessee

[4]Department of Physics, Federal Institute of Pará, Belém, Brazil

[5]Institute for Atmospheric and Earth System Research/Physics, Faculty of Science, University of Helsinki, Helsinki, Finland

Correspondence
Luca Mortarini, Università di Milano, Dipartimento di Scienze della Terra 'Ardito Desio', Milan 20133, Italy.
Email: luca.mortarini@unimi.it

Funding information
Instituto Nacional de Pesquisas da Amazônia (INPA), the Max-Planck Society, the German Federal Ministry of Education and Research (BMBF Contract Nos. 01LB1001A, 01LK1602A, and 01LK1602B), the Brazilian Ministério da Ciência, Tecnologia e Inovação (MCTI/FINEP Contract No. 01.11.01248.00), the Amazon State University (UEA), FAPEAM, CAPES and SDS/CEUC/RDS-Uatumã; NRC Research Associateship Program at Air Resources Laboratory, National Oceanic and Atmospheric Administration, administered by the Fellowships Office of the National Academies of Sciences, Engineering, and Medicine; CNPq's (307530/2022-1; 406884-2022-6). U.S. National Science Foundation (NSF-AGS-2028633, and the Department of Energy (DE-SC0022072). ICOS-FI via University of Helsinki funding and the EU Horizon Europe Framework Programme for Research and Innovation (GreenFeedback nr. 101056921)

Abstract

The influence of thermal stratification on the turbulent kinetic energy balance has been widely studied; however, its influence on the turbulent stress remains less explored in the presence of tall vegetated canopies and less ideal micrometeorological conditions. Here, the impact of thermal stratification on turbulent momentum flux is considered in the roughness sublayer (RSL) and the atmospheric surface layer (ASL) using the Amazon Tall Tower Observatory (ATTO) in Brazil. A scale-wise co-spectral budget (CSB) model is developed using standard closure schemes for the pressure–velocity decorrelation. The CSB revealed that the co-spectrum $F_{wu}(k_x)$ between longitudinal (u') and vertical (w') velocity fluctuations is impacted by the energy spectrum of the vertical velocity $E_{ww}(k_x)$ and the much less studied longitudinal heat-flux co-spectrum $F_{u\theta_v}(k_x)$, where θ_v' are temperature fluctuations and k_x is the longitudinal wavenumber. Under stable, very stable, and dynamic–convective conditions, the scaling exponent in $F_{wu}(k_x)$ for the inertial subrange (ISR) scales is dominated by $F_{u\theta_v}(k_x)$ instead of $E_{ww}(k_x)$. A near $k_x^{-7/3}$ scaling in $F_{u\theta_v}(k_x)$ robust to large variations in thermal stratification is found, whereas the Kolmogorov ISR scaling for $E_{ww}(k_x) \sim k_x^{-5/3}$ is not found. The scale-dependent decorrelation time between u' and w' is dominated by $\epsilon^{-1/3}k_x^{-2/3}$ in the ISR, but is nearly constant for eddies larger than the vertical velocity integral scale, regardless of stability. Implications of these findings for generalized stability correction functions that are based on the turbulent stress budget instead of the turbulent kinetic energy budget are discussed.

KEYWORDS

Amazon Tall Tower Observatory, canopy turbulence, co-spectral budget model, horizontal turbulent heat flux, momentum transport, roughness sublayer

1 INTRODUCTION

The significance of thermal stratification on momentum transport within the roughness sublayer (RSL) and the atmospheric surface layer (ASL) above tall and dense canopies is not in dispute and continues to draw significant attention. This attention is partly motivated by practical needs, such as subgrid-scale schemes for large-eddy simulations (LES), now being applied to wide-ranging diabatic conditions in the atmosphere (Wyngaard, 2010), or correcting unresolved scales in turbulent stress measurements (Cava & Katul, 2012). At a more basic level, identifying how different eddy sizes that transport momentum are impacted by thermal stratification relative to their neutral counterparts enables refined stability correction functions to be derived (Katul *et al.*, 2011; Li *et al.*, 2016), beyond those described by the much-studied Monin–Obukhov similarity theory (MOST: Monin & Obukhov, 1954). Another variant on this problem is the use of the so-called Reynolds analogy to relate turbulent momentum and heat transfer (Li, 2019). This analogy argues that, in the vertical direction, momentum and heat are transported identically by the same eddies, thereby resulting in a constant turbulent Prandtl number. However, when buoyancy is driving turbulent kinetic energy generation or destruction at scales different from those responsible for mechanical stress production, this analogy breaks down (Katul *et al.*, 2014).

The rough but porous surface of tall forested canopies distorts atmospheric flows by modifying the flow statistics above the canopy in ways that differ from canonical rough-wall boundary layers. Because the mean flow velocity is finite and turbulence remains energized at multiple length-scales within the canopy, a RSL is established whereby canopy effects can permeate up to twice the canopy height above the forest floor. According to the mixing-layer analogy (Raupach *et al.*, 1996) for the RSL, hydrodynamic instabilities associated with the inflection point in the mean velocity profile near the canopy top give rise to three-dimensional coherent structures (Finnigan *et al.*, 2009) that cannot form in canonical wall-bounded flows. These coherent structures are organized in cycles of ejections (weak rising motions) and sweeps (energetic and intermittent downward gusts) and are responsible for many of the momentum and scalar exchanges between the biosphere and the atmosphere. Further, being efficient in mixing and transporting momentum, canopy coherent structures can sustain fluxes with smaller than inertial gradients (Brunet, 2020), implying a failure of MOST even in the neutral limit (Cava *et al.*, 2006; Chamecki *et al.*, 2020; Dias-Júnior *et al.*, 2019; Katul & Albertson, 1999; Siqueira *et al.*, 2000; Siqueira & Katul, 2002). This failure necessitates modified flux-gradient relations that take RSL effects into account (Harman & Finnigan, 2007, 2008). The ability of canopy-scale eddies to penetrate all the way down to the forest floor has also recently been related to the intermittent nature of momentum transfer close to the canopy top (Chowdhuri *et al.*, 2022), thereby making the study of scalewise momentum transport just above the canopy and in the ASL necessary for understanding the complex processes near the forest floor.

In neutral stratification, the validity of the mixing-layer analogy has been assessed (Brunet & Irvine, 2000; Shaw *et al.*, 1995). It was shown through flume experiments on rod canopies of varying densities that averaged flow statistics near the canopy top experience both Kelvin–Helmholtz and attached eddies (Poggi *et al.*, 2004a). However, the impact of atmospheric stability on the RSL flow dynamics in general and momentum transfer in particular is less understood (Dupont & Patton, 2012a, 2012b). In diabatic conditions, other mechanisms such as thermal plumes (unstable) and submeso motions (very stable) can influence the momentum exchange above and inside the forest, even more so than mixing-layer type coherent structures. In unstable conditions, thermal plumes and coherent vortices having different temporal and spatial scales may coexist (Thomas *et al.*, 2006), while in stable stratification low-frequency submeso structures propagate downward (Cava *et al.*, 2022), disrupting the RSL dynamics (Corrêa *et al.*, 2021). Figure 1 provides a graphical representation summarizing the atmospheric layer structure above a tall forest under neutral, unstable, and stable stratification. Defining δ as the boundary-layer height and h as the canopy height, the neutral schematic features a canonical case where the roughness sublayer extends from $z/h = 1$–2 for momentum, the inertial sublayer extends from $z/h > 2$ but for $z/\delta < 0.2$, and the outer layer extends from $z/\delta > 0.2$ to the boundary-layer top $z/\delta \approx 1$. The unstable schematic presents the possible erosion of the inertial sublayer hypothesized elsewhere (Dias-Júnior *et al.*, 2019) with increasing instability, while the stable schematic presents the very stable case where low-frequency structures from the outer layer propagate downward with increasing stability and erode both the inertial sublayer and the roughness sublayer (Cava *et al.*, 2022; Mendonça *et al.*, 2025). Thus, z/h may no longer be an adequate indicator separating ASL from RSL.

One challenge to exploring the role of thermal stratification on momentum transfer is that thermal stratification does not appear explicitly in the mean momentum balance along the longitudinal direction. It appears indirectly through its effects on the mean pressure gradient driving the flow. Thus, to elucidate the buoyancy contribution to momentum transfer, it is necessary to consider the turbulent stress budget directly (Garratt, 1992; Kaimal &

Quarterly Journal of the Royal Meteorological Society RMetS

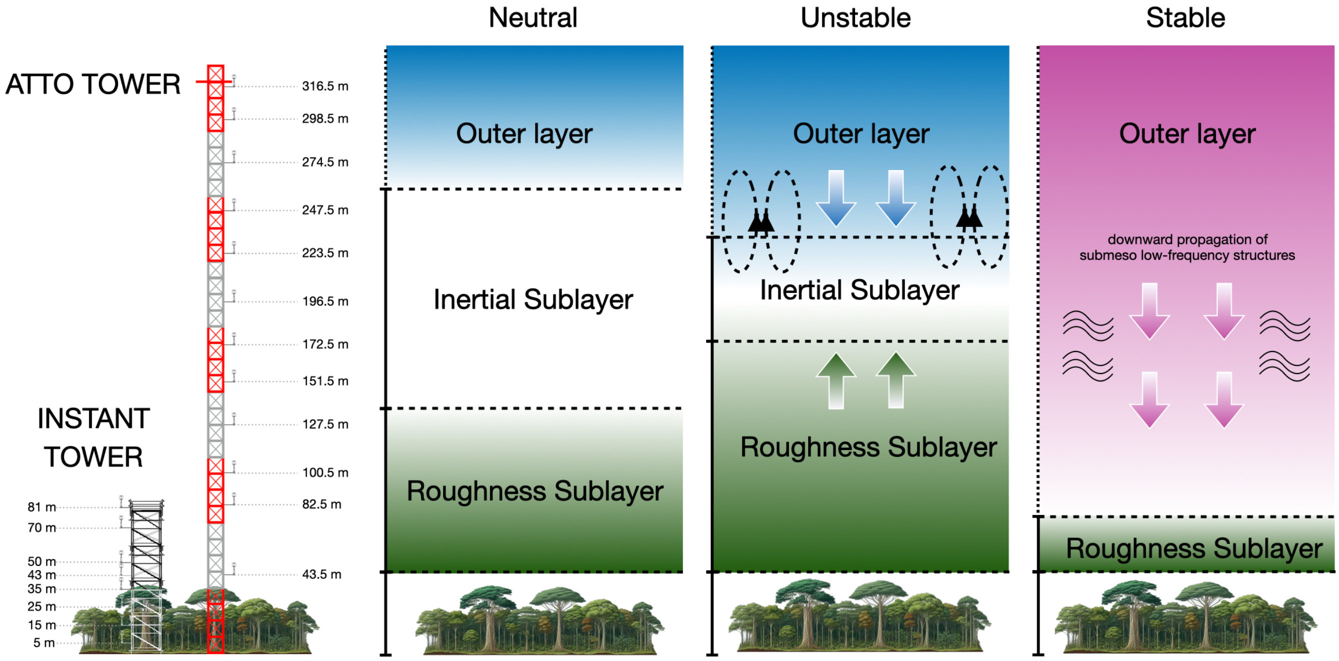

FIGURE 1 Experimental setup at the ATTO site showing sensor locations on both the INSTANT tower and the tall ATTO tower (left). One tower (INSTANT) investigates the roughness sublayer, whereas the tall tower (ATTO) investigates all three layers—the RSL, the inertial sublayer, and the outer layer—albeit at a coarser vertical resolution. The schematics illustrate the approximate extent of the roughness, inertial, and outer layers under different stratification conditions: neutral, unstable, and stable. The boundary-layer height (not shown) is different across these stability classes. For very stable and dynamic–convective conditions, z/h may no longer serve as an acceptable indicator of RSL versus ASL flows. The height of the tallest tree represents the canopy height, h (= 37 m here). [Colour figure can be viewed at wileyonlinelibrary.com]

Finnigan, 1994). As with all Reynolds-averaged equations, such budgets are intended to assess the dominant mechanisms but do not contain any distinct eddy sizes or scale information beyond some externally supplied length- or time-scale. To explore what scales are excited by the mechanical production term and what scales are excited or dampened by buoyancy and how those two processes interact spectrally when describing scalewise momentum transfer requires approaches that go beyond Reynolds-averaged equations. A possible way forward that accommodates all the length-scales involved is a co-spectral budget (CSB) model introduced elsewhere (Katul *et al.*, 2013a). In neutral conditions, the CSB was shown to provide a form of eddy viscosity, ν_T, that depends on the scalewise integrated energy spectrum of the vertical velocity and thus applies simultaneously in the RSL and the inertial sublayer (Mortarini *et al.*, 2023). The work here goes beyond those recent attempts and explores the effects of atmospheric stratification on the scalewise momentum transport above a tall forested canopy at an Amazon site in Brazil. Four months of data collected at the Amazon Tall Tower Observatory (ATTO) site at five different heights between March and June 2023 were analyzed. These heights span the RSL and ASL, as shown in Figure 1. It is envisaged that the proposed analysis forms an embryonic step to deriving generalized stability correction functions capable of accommodating all the scales of motion across wide-ranging diabatic conditions in the atmosphere above tall forested canopies.

2 | THEORY

The role of buoyancy in the ASL has been conventionally studied using the turbulent kinetic energy (TKE) budget. For this reason, the salient features of the turbulent kinetic energy and turbulent stress budgets are first reviewed, highlighting key differences between them. Moreover, the basic closure schemes to be employed scalewise in the co-spectral budget later on are covered.

2.1 | General definitions

For a stationary and planar homogeneous flow at high Reynolds number in the absence of subsidence, the turbulent stress budget is (Garratt, 1992; Kaimal & Finnigan, 1994; Wyngaard, 2010)

$$\frac{\partial \overline{w'u'}}{\partial t} = 0 = -\sigma_w^2 \Gamma(z) + R_{u,w} + \beta_o \overline{u'\theta_v'} - \left[\frac{\partial \overline{w'w'u'}}{\partial z} + 2\epsilon_{uw}\right], \tag{1}$$

where t is time, z is the vertical distance from the ground or forest floor, the overline indicates averaging over coordinates of statistical homogeneity (commonly time averaging), u' and w' are the longitudinal (along x) and vertical (along z) velocity fluctuations around their mean states $\overline{U}$ and $\overline{W}=0$ (no subsidence), $\sigma_w^2=\overline{w'^2}$ is the vertical velocity variance, $\Gamma=\partial\overline{U}/\partial z$ is the mean longitudinal velocity gradient, $\overline{w'w'u'}$ is the vertical transport of $u'w'$ by turbulence, $R_{u,w}$ is the pressure–rate-of strain decorrelation, ϵ_{uw} is the decorrelation of u' from w' due to the action of viscosity, $\beta_o=g/\overline{\theta_v}$ is the buoyancy parameter, with g being the gravitational acceleration and $1/\overline{\theta_v}$ being the coefficient of thermal expansion of an ideal gas (air), θ_v' is the virtual temperature fluctuation around its mean state $\overline{\theta}_v$, and $\overline{u'\theta_v'}$ is the horizontal heat flux, which can be positive or negative. For comparison, the TKE budget for the same idealized conditions is given by

$$\frac{\partial\overline{e}}{\partial t}=0=-\overline{u'w'}\Gamma(z)+\beta_o\overline{w'\theta_v'}-\epsilon-\left[\frac{\partial\overline{w'e}}{\partial z}+\frac{\partial\overline{w'p'}}{\partial z}\right],\tag{2}$$

where $e=(1/2)(u'u'+v'v'+w'w')$ is the instantaneous TKE, and p' is the pressure perturbation from a hydrostatic state normalized by density. As in the stress budget, the terms on the right-hand side are, respectively, mechanical production, buoyant production or destruction due to vertical heat transport, turbulent kinetic energy dissipation rate due to the action of viscosity ($=\epsilon$), and the two transport terms lumped together in the bracketed quantity: turbulent transport of TKE and pressure diffusion of TKE. The turbulent transport and pressure diffusion do not contribute to the generation or destruction of TKE, only its transport across different regions.

The dominant terms in both budgets are reviewed briefly. In the stress budget, ϵ_{uw} is minor compared with $R_{u,w}$, whereas ϵ can far exceed the pressure diffusion term in the TKE budget (Kaimal & Finnigan, 1994). Very fine-scale eddies, such as those commensurate to the Kolmogorov microscale $\eta_K=(\nu^3/\epsilon)^{1/4}$, play a different role in these two budgets, where ν is the molecular viscosity. For the TKE budget, the ultimate conversion of the kinetic energy produced and transferred down across scales (i.e., ϵ) to heat occurs in these isotropic micro-eddies. However, at the same micro-scales dissipating TKE, u' is already decorrelated from w' due to $R_{u,w}$. The ϵ_{uw} is thus acting on a residual stress term that is already small in magnitude given the near-isotropic nature of η_K. To elaborate further on the role of the pressure–velocity interaction terms in the two budgets, the pressure redistribution term acts on the individual velocity variances (i.e., σ_u^2, σ_v^2, and σ_w^2), with the goal of making the energy equipartitioned among velocity components. However, the pressure redistribution terms do not contribute to the generation or destruction of TKE. This is in stark contrast to $R_{u,w}$, which acts as a primary decorrelation term for u' from w' that is far more efficient than viscous effects. In the ASL and for both budgets, the transport by turbulence is also assumed to be small compared with the mechanical production terms (Charuchittipan & Wilson, 2009; Garratt, 1992; Kaimal & Finnigan, 1994). For this reason, it is customary to neglect the bracketed quantities in both budgets. In the context of the stress budget and stratified flow, ignoring the flux-transport term warrants further discussion. In the RSL for near-neutral flows, the flux-transport term may not be small, as already shown experimentally for a rod canopy in a flume (Poggi *et al.*, 2004b) and many field experiments reviewed elsewhere (Katul & Albertson, 1998). To leading order, $\overline{w'w'u'}$ is expected to scale with $d(\overline{w'u'})/dz$, as is common to virtually all higher order closure schemes (Corrsin, 1975; Launder *et al.*, 1975; Wilson & Shaw, 1977). For very stable and very unstable conditions, $|\overline{w'u'}|$ may not be large in both the RSL and ASL compared with the near-neutral case. If so, then $d\overline{w'u'}/dz$ and likely $d(\overline{w'w'u'})/dz$ may be small compared with the buoyancy term in the stress budget.

2.2 | Two perspectives on thermal stratification

In virtually all textbooks today (Kaimal & Finnigan, 1994), the flux Richardson number Ri_f, or alternatively the stability parameter ζ associated with MOST (Monin & Obukhov, 1954), is used to assess the importance of buoyancy on flow statistics. Optimism about MOST capturing the effects of buoyancy on many flow statistics emerged shortly after the Kansas experiment. This optimism is perhaps best summarized by the following statement from Kaimal (1973) "*…with proper non-dimensionalization, all flow statistics in the surface layer can be reduced to a set of universal curves*". To be clear, the MOST definitions and non-dimensionalization originate from the TKE budget and not the stress budget. Inspecting the TKE budget, the parameters Ri_f and ζ are defined and related by

$$Ri_f=\frac{\beta_o\overline{w'\theta_v'}}{[\overline{u'w'}\Gamma(z)]}=-\frac{\zeta}{\phi_m(\zeta)};\qquad \zeta=\frac{z-d_o}{L_o},$$
$$L_o=\frac{-u_*^3}{\kappa\beta_o\overline{w'\theta_v'}};\qquad \phi_m(\zeta)=\Gamma(z)\frac{\kappa(z-d_o)}{u_*},\tag{3}$$

where u_* is the friction velocity, d_o is the zero-plane displacement, κ is the von Kármán constant, L_o is the Obukhov length, and $\phi_m(\zeta)$ is the MOST stability correction function. For unstable stratification (land surface heating up), $\overline{w'\theta_v'} > 0$, $\zeta < 0$, and $\phi_m(\zeta) < 1$, whereas for stable stratification (land surface cooling down) $\overline{w'\theta_v'} < 0$, $\zeta > 0$, and $\phi_m(\zeta) > 1$. Such conventional assessment of buoyancy originating from the TKE budget need not apply to the stress budget. In the stress budget, a logical Richardson-like number would be $\beta_o\overline{u'\theta_v'}/[\overline{w'w'}\Gamma(z)]$ instead of Ri_f. Likewise, as with the definition of L_o, it is possible to define a new length-scale reflecting the contribution of mechanical production and buoyancy production (or destruction) terms to the turbulent stress budget (hereafter labeled as L_{sb}). This new length L_{sb} is given as

$$L_{sb} = \frac{\sigma_w^2 u_*}{\kappa\beta_o\overline{u'\theta_v'}}\phi_m(\zeta). \tag{4}$$

As with L_o and vertical sensible heat flux, when $\overline{u'\theta_v'} \to 0$, $L_{sb} \to \infty$. Moreover, a stability parameter associated with the stress budget may also be defined as $\zeta_{sb} = (z - d_0)/L_{sb}$, and this may be better suited than ζ for analyzing momentum transport and turbulent stresses. When $\zeta_{sb} \to 0$, thermal stratification can be ignored in the stress budget, and when $\zeta_{sb} \to \infty$, buoyancy dominates the stress and gradient-diffusion models linking $\overline{w'u'}$ to Γ may fail spectacularly, as shown later. Also, L_{sb} is not independent from ζ, as both $(\sigma_w/u_*)^2$ and $\phi_m(\zeta)$ vary with ζ.

2.3 | A simplified turbulent stress budget

Upon ignoring (i) the flux transport relative to the mechanical production of the turbulent stress $(-\sigma_w^2\Gamma)$ and (ii) the viscous decorrelation term relative to $R_{u,w}$ (Katul *et al.*, 2013a; Mortarini *et al.*, 2023), and upon using a conventional Rotta return-to-isotropy closure scheme to represent $R_{u,w}$ corrected for the isotropization of the production, the turbulent stress budget reduces to

$$-(1 - C_I)\sigma_w^2\Gamma(z) - C_R\frac{\overline{w'u'}}{\tau} + (1 - C_I)\beta_o\overline{u'\theta_v'} = 0, \tag{5}$$

where $C_I = 3/5$ is a constant associated with the fast isotropization of the production term, the numerical value of which has been derived from rapid distortion theory (Katul *et al.*, 2013a; Pope, 2000), $C_R = 1.8$ is the Rotta constant associated with the slow pressure–rate-of-strain part (Pope, 2000), and τ is a decorrelation time-scale that may be related to a relaxation time (to be discussed later). The so-called LRR-IP model for $R_{u,w}$ (after Launder, Reece, and Rodi including the isotropization of the production) has been chosen, because it reproduces the mean velocity and stresses in various types of shear flows (Choi & Lumley, 2001; Durbin, 1993; Hanjalić & Launder, 2021; Launder *et al.*, 1975; Pope, 2000). We wish to draw attention to the fact that the isotropization of the production here applies to the production terms in the turbulent stress budget (i.e., $-\sigma_w^2\Gamma + \beta_o\overline{u'\theta_v'}$). When analyzing the return to isotropy in the componentwise velocity variance budgets separately, the rapid part of the pressure–strain interaction acts on the mechanical production in the σ_u^2 budget and on $\beta_o\overline{w'\theta_v'}$ in the σ_w^2 budget. In the individual velocity variance budgets, the return to isotropy (slow and rapid) arising from the pressure–velocity interaction terms acts as a "Robin Hood" effect, taking energy from the energy-rich velocity component and distributing it to the energy-poor velocity components. In the stress budget, the return-to-isotropy term is acting to decorrelate u' from w' (i.e., return to isotropy) and its rapid contribution seeks to weaken sources that generate a covariance between u' and w'.

Returning to the stress budget, Equation (5) can be written as

$$\overline{w'u'} = -\nu_T\Gamma(z) + \left[\frac{\tau}{A}\beta_o\overline{u'\theta_v'}\right], \tag{6}$$

where $A = C_R/(1 - C_I) = 4.5$ and $\nu_T = A^{-1}(\tau\sigma_w^2)$ is a turbulent or eddy viscosity. The first term is a conventional gradient-diffusion closure to the turbulent stress $\overline{w'u'}$ (Pope, 2000), whereas the second term is an additive correction arising from buoyancy. Due to its simplicity, Equation (6) carries the novelty of a turbulent momentum budget approach. As a matter of fact, two dynamically interesting corollaries emerge from it.

(i) The horizontal heat-flux buoyancy term can be positive or negative depending on the sign of $\overline{u'\theta_v'}$. When the buoyancy correction term is large, $\overline{w'u'}$ may no longer be related to or even explained by the mean velocity gradient Γ and thus gradient diffusion (sometimes referred to as K-theory) breaks down. This "breakdown" of K-theory cannot be attributed to the flux-transport term as often stated in the literature (Corrsin, 1975). Instead, it is driven entirely by thermal stratification in the context of the turbulent stress budget. As a comparison, consider the standard eddy viscosity ν_T defined by MOST as (Brutsaert, 1982)

$$\nu_T = \frac{\kappa(z - d_o)u_*}{\phi_m(\zeta)}. \tag{7}$$

The contributions of various eddy sizes to the vertical (or sensible) heat flux $\overline{w'\theta_v'}$ may not be identical to those that contribute to $\overline{u'\theta_v'}$. Such dissimilarity between these two heat fluxes complicates any link between $\overline{w'u'}$ and Γ, which is one of the main motivations for the work here. Long-term experiments (Kader & Yaglom, 1990) already suggest complex and non-monotonic scaling with ζ for the ratio of these two heat fluxes in unstable conditions. Specifically, $\overline{u'\theta_v'}/\overline{w'\theta_v'}$ in unstable conditions exhibits the following behavior: for near-neutral to mildly unstable flows, $\overline{u'\theta_v'}/\overline{w'\theta_v'} > 4$, but it then drops below unity around $\zeta = -1$, and experiences a rebound and continues to increase with decreasing ζ for near-convective conditions (Kader & Yaglom, 1990).

(ii) Above the canopy but within the RSL, it is safe to assume that the turbulent momentum flux is negative, and hence

$$-\sigma_w^2 \frac{dU}{dz} + \frac{g}{\overline{\theta}_v}\overline{u'\theta_v'} \leq 0. \tag{8}$$

In stable stratification in which $\overline{u'\theta_v'}$ is positive,

$$\overline{u'\theta_v'}_{\mathrm{vmax}} = \frac{\overline{\theta}_v}{g}\,\sigma_w^2 \frac{dU}{dz}. \tag{9}$$

This $\overline{u'\theta_v'}$ represents the maximum sustainable horizontal heat flux in the absence of a momentum flux. The concept of maximum sustainable (vertical) heat flux was already introduced van de Wiel *et al.* (2007) and de Wiel *et al.* (2012a, 2012b). These studies showed that the downward heat flux in a stably stratified flow is limited to a certain maximum (Katul *et al.*, 2014). This is the maximum surface heat extraction that the turbulence can support. Above this limit, turbulence is unable to survive in its fully developed state. When assuming $\overline{u'\theta_v'} = -\alpha_\theta \overline{w'\theta_v'}$, where α_θ is a constant, then the predicted maximum downward heat flux is

$$\overline{w'\theta_v'}_{\mathrm{vmax}} \geq -\frac{1}{\alpha_\theta}\frac{\overline{\theta}_v}{g}\,\sigma_w^2 \frac{dU}{dz}. \tag{10}$$

While Equation (5) presents the dominant balance among the processes governing $\overline{u'w'}$, it lacks explicit information on eddy sizes or scale contributions to momentum transport. Consequently, determining the scales that are energized by mechanical production and how they are influenced by (longitudinal) buoyancy, and how these two processes interact spectrally to shape the overall momentum flux, remains hidden from Equation (5). The goal now is to explore such scalewise effects of buoyancy (through the horizontal heat flux) on the co-spectrum of $\overline{w'u'}$ and to interpret the findings using such an idealized budget for both unstable and stable conditions where the dominant mechanisms remain as in Equation (5).

2.4 | The co-spectral budget (CSB) model

The momentum flux $\overline{w'u'}$, the vertical velocity variance σ_w^2, the longitudinal velocity variance σ_u^2, and the longitudinal heat flux $\overline{u'\theta_v'}$ can be linked to eddy sizes or scales using the *integral* properties:

$$\overline{w'u'} = -\int_0^\infty F_{wu}(k_x)dk_x, \qquad \overline{w'w'} = \int_0^\infty E_{ww}(k_x)dk_x,$$
$$\overline{u'u'} = \int_0^\infty E_{uu}(k_x)dk_x, \qquad \overline{u'\theta_v'} = -\int_0^\infty F_{u\theta_v}(k_x)dk_x, \tag{11}$$

where $F_{wu}(k_x)$ and $F_{u\theta_v}(k_x)$ are the turbulent stress and longitudinal heat-flux co-spectra, while $E_{ww}(k_x)$ and $E_{uu}(k_x)$ are the vertical velocity and longitudinal velocity spectra. These co-spectra and spectra are all defined using the longitudinal wavenumber k_x along the mean wind direction x when employing Taylor's frozen turbulence hypothesis (Taylor, 1938; Wyngaard & Clifford, 1977).

A minimalist CSB model for $F_{wu}(k_x)$ can be derived to link $F_{wu}(k_x)$ explicitly to $E_{ww}(k_x)$ and $F_{u\theta_v}(k_x)$ at each wavenumber or scale by Fourier-transforming Equation (1). This transformation yields (Bos *et al.*, 2004; Katul *et al.*, 2013b)

$$\frac{\partial F_{wu}(k_x)}{\partial t} + 2\nu k_x^2 F_{wu}(k_x) = P_{wu}(k_x) + T_{wu}(k_x) + \pi(k_x) + \beta_o F_{u\theta_v}(k_x), \tag{12}$$

where $\epsilon_{wu} = 2\nu\int_0^\infty k_x^2 F_{wu}(k_x)dk_x$ is the decorrelation of the turbulent stress by the action of the molecular viscosity ν, $P_{wu}(k_x) = -\Gamma(z)E_{ww}(k_x)$ is the mechanical production of the shear stress responsible for generating the covariance between u' and w' due to a finite mean velocity gradient, $T_{wu}(k_x)$ is the co-spectral momentum flux transfer (not kinetic energy transfer) across scales, and $\pi(k_x)$ is the scalewise velocity–pressure interaction term and is related to the pressure–rate-of-strain $R_{u,w}$. For stationary and planar homogeneous flows in the *inertial sublayer*, neglecting the decorrelation due to viscous effects and $T_{wu}(k_x)$ relative to $\pi(k_x)$, Equation (12) reduces to

$$0 \approx -\Gamma(z)E_{ww}(k_x) + \pi(k_x) + \beta_o F_{u\theta_v}(k_x). \tag{13}$$

A plausibility argument for ignoring $T_{wu}(k)$ relative to $\pi(k)$ is from direct numerical simulations (DNS) (Bos *et al.*, 2004) and other scaling arguments (Katul *et al.*, 2013a) discussed later on with regard to scaling exponents of $F_{wu}(k_x)$ in the inertial subrange (ISR). To establish a relation between $\Gamma(z)$, $E_{ww}(k_x)$, and $F_{wu}(k_x)$ based on Equation (12), a closure for the pressure–velocity co-spectrum $\pi(k_x)$ is again needed.

2.5 | A spectral closure for the pressure decorrelation

To investigate the effects of atmospheric stability on the CSB model scale by scale, two closure schemes for $\pi(k_x)$ are introduced. One scheme ignores the thermal stratification altogether and is labeled as π_{neutral}, while the other assumes thermal stratification impacts the rapid term and is labeled as π_{diabatic}. Both schemes must include the slow Rotta contribution to $F_{wu}(k_x)$. The rapid isotropization of the production term acts only on the mechanical production of the stress in π_{neutral}, whereas it acts on both the mechanical and buoyancy terms in π_{diabatic}. These two schemes are thus given by (Ayet *et al.*, 2020; Besnard *et al.*, 1996; Launder *et al.*, 1975; Pope, 2000)

$$\pi_{\text{neutral}}(k_x) = -C_{\text{R}}\frac{F_{wu}(k_x)}{\tau(k_x)} + C_{\text{I}}E_{ww}(k_x)\Gamma(z), \tag{14}$$

$$\pi_{\text{diabatic}}(k) = -C_{\text{R}}\frac{F_{wu}(k_x)}{\tau(k_x)} + C_{\text{I}}\left[E_{ww}(k_x)\Gamma(z) - \beta_{\text{o}}F_{u\theta_{\text{v}}}(k_x)\right], \tag{15}$$

where $\tau(k_x)$ is interpreted as a scale-dependent decorrelation time-scale, assumed to be similar in both formulations. It is to be noted that the isotropization of the production or the rapid part used here acts directly on terms in the stress budget and not on component-wise velocity variance budgets. In the ISR that delineates scales much smaller than the integral length but much larger than η_{K}, the following results are expected to hold (Kolmogorov, 1941):

$$E_{ww}(k_x) = C_{\text{o},w}\epsilon^{2/3}k_x^{-5/3};\ \tau(k_x) = \alpha\epsilon^{-1/3}k_x^{-2/3}, \tag{16}$$

where $C_{\text{o},w} = (24/55)C_{\text{K}}$ is the Kolmogorov constant for the vertical velocity, with $C_{\text{K}} = 1.5$ being the Kolmogorov constant associated with three-dimensional wavenumber space, and α is a proportionality constant of order unity. Under this closure assumption, the CSB model for $F_{wu}(k_x)$ reduces to

$$-(1 - C_{\text{I}})\Gamma(z)E_{ww}(k_x) - \frac{C_{\text{R}}}{\tau(k_x)}F_{wu}(k_x) + (1 - C_{\text{I}})\beta_{\text{o}}F_{u\theta_{\text{v}}}(k_x) = 0. \tag{17}$$

The co-spectrum $F_{wu}(k_x)$ can be expressed as

$$-F_{wu}(k_x) = \frac{1}{A}\tau(k_x)\left[\Gamma(z)E_{ww}(k_x) - \beta_{\text{o}}F_{u\theta_{\text{v}}}(k_x)\right]. \tag{18}$$

When setting $F_{u\theta_{\text{v}}}(k_x) = 0$ and focusing on the ISR,

$$F_{wu}(k_x) = -\frac{1}{A}\tau(k_x)\Gamma(z)E_{ww}(k_x). \tag{19}$$

Inserting the ISR formulations for $E_{ww}(k_x) = C_{\text{o},w}\epsilon^{2/3}k_x^{-5/3}$ and $\tau(k_x) = \alpha\epsilon^{-1/3}k_x^{-2/3}$ with $\alpha = 1$ yields (Katul *et al.*, 2013a)

$$F_{wu}(k_x) = -C_{uw}\left[\epsilon^{1/3}k_x^{-7/3}\right]\Gamma, \tag{20}$$

where $C_{uw} = C_{\text{o},w}/A$. This expression is identical to the textbook formulation of $F_{wu}(k_x)$ (Kader & Yaglom, 1991; Lumley, 1967; Pope, 2000; Saddoughi & Veeravalli, 1994) and those derived from dimensional considerations alone (Bos *et al.*, 2004; Cava & Katul, 2012), but with one notable exception. The numerical value of C_{uw} here is theoretically predicted to be $C_{uw} = 0.65/4.5 = 0.145$. This numerical value is in agreement with the Kansas experiment, wind-tunnel studies, and DNS that report C_{uw} to be empirically between 0.14 and 0.16 (Katul *et al.*, 2013a). A more dynamically interesting implication of Equation (20) is that, when measured $F_{wu}(k_x)$ in the ISR is shown empirically to scale as $k_x^{-7/3}$, the contributions of the flux transfer term $T_{wu}(k_x)$ cannot be large and may be ignored altogether (Li & Katul, 2017), given that $\int_0^\infty T_{wu}(k_x)dk_x = 0$. While local isotropy has been shown to be achieved in the ISR of velocity spectra (Saddoughi & Veeravalli, 1994), strict isotropy here requires that $F_{wu}(k_x)$=0. $F_{wu}(k_x)$=0 can only be achieved when $\Gamma = 0$ as $\epsilon > 0$ to sustain turbulence. Nonetheless, $|F_{wu}(k_x)|$ decays rapidly $(-7/3)$ with increasing k_x, and is likely to be trivial in the vicinity of $k_x\eta = 1$, supporting the simplification of ignoring $2\nu k_x^2F_{uw}(k_x)$ relative to the pressure decorrelation.

2.6 | Further remarks on the longitudinal heat flux ISR co-spectral scaling

Using $\pi_{\text{diabatic}}(k_x)$ adds a layer of complexity that is difficult to analyze even for the much-studied ISR. That $F_{wu}(k_x)$ now depends on $F_{u\theta_{\text{v}}}(k_x)$ poses significant challenges to its scalewise modeling, as the scaling laws describing $F_{u\theta_{\text{v}}}(k_x)$ are not well constrained or agreed upon.

To underscore this point, $F_{u\theta_{\text{v}}}(k_x)$ can be expressed as k_x^{-m} in the ISR identified by velocity spectra and the values of m are now reviewed. Early studies from the Kansas experiment report values anywhere from $m = 3$ (Wyngaard & Coté, 1972) to $m = 5/2$ (Kaimal *et al.*, 1972). However, the experiments in Minnesota suggest $m = 7/3$ (Caughey *et al.*, 1979). The long-term experiments at Tsimlyansk (Russia) also point towards $m = 7/3$ (Kader & Yaglom, 1991). Wind-tunnel experiments where temperature can be assumed as a passive scalar (Antonia & Zhu, 1994) report $m = 5/3$ for some three decades of k_x, before transitioning in a very narrow range of scales to $m = 7/3$ followed by an exponential cutoff. Studies in the roughness sublayer of an alpine forest (Cava &

TABLE 1 Summary of reported values of the scaling exponent for $F_{u\theta_v}(k_x) \sim k_x^{-m}$ in the ISR.

Experiment	Methodology	Reported *m*
Kansas experiment	Atmospheric measurements	3 (Wyngaard & Coté, 1972) to 5/2 (Kaimal *et al.*, 1972)
Minnesota experiment	Atmospheric measurements	7/3 (Caughey *et al.*, 1979)
Tsilymansk experiment	Atmospheric measurements	7/3 (Kader & Yaglom, 1991)
Laboratory experiment	Wind tunnel	5/3 (three decades of k_x), then 7/3 with cutoff (Antonia & Zhu, 1994)
Lavarone experiment	Atmospheric measurements	7/3 (for at least two decades of wavenumbers) (Cava & Katul, 2012)
Numerical experiment	Direct numerical simulation	2 (Bos *et al.*, 2004)

Katul, 2012) in Lavarone (Italy) spanning both unstable and mildly stable conditions suggest $m = 7/3$ for at least two decades of wavenumbers in the ISR. These experiments, summarized in Table 1, also suggest that some deviations from $k_x^{-5/3}$ in $E_{ww}(k_x)$ may only partly explain deviations from $k_x^{-7/3}$ in $F_{wu}(k_x)$, but not all of them. DNS (Bos *et al.*, 2004) suggest $m = 2$, attributing the deviations from $m = 7/3$ to the finite flux transfer across scales (i.e., $T_{uw}(k_x)$). Unlike ϵ, the flux transfer associated with the longitudinal heat flux across k_x is not a "conserved" quantity and thus exhibits its own exponent.

To provide a plausibility argument for the many reported scaling laws governing $F_{u\theta_v}(k_x)$ in the ISR, dimensional analysis can be used with the following list of variables (Bos *et al.*, 2004; Cava & Katul, 2012): (i) k_x, (ii) mean gradients of u (i.e., Γ) and θ_v (i.e., $\Gamma_\theta = \partial\overline{\theta_v}/\partial z$), and (iii) conservative quantities in the energy and temperature variance cascades, such as ϵ and the temperature variance dissipation rate (ϵ_θ). With this list, it is straightforward to show the following.

- When $F_{u\theta_v}(k_x)$ is assumed to vary with k_x, ϵ, and ϵ_θ (i.e., no mean gradients), dimensional analysis requires that $F_{u\theta_v}(k_x) \sim \epsilon_\theta^{1/2}\epsilon^{1/6}k_x^{-5/3}$.
- When $F_{u\theta_v}(k_x)$ is assumed to vary with k_x and mean gradient quantities only (i.e., Γ and Γ_θ), then $F_{u\theta_v}(k_x) \sim (\Gamma)(\Gamma_\theta)k_x^{-3}$.
- When $F_{u\theta_v}(k_x)$ is assumed to vary with k_x, ϵ_θ, and Γ (i.e., mixed quantities), then $F_{u\theta_v}(k_x) \sim (\Gamma\epsilon_\theta)^{1/2}k_x^{-2}$.
- When $F_{u\theta_v}(k_x)$ is assumed to vary with k_x, ϵ, and Γ_θ (another mixed quantity), then $F_{u\theta_v}(k_x) \sim \Gamma_\theta\epsilon^{1/3}k_x^{-7/3}$.

Experimentally however, it is difficult to discern differences between $k_x^{-7/3}$ and $k_x^{-6/3}$. Nonetheless, it is safe to state that mixed variables are expected to govern the longitudinal heat-flux co-spectrum when the measured ISR scaling exponents are near $-6/3$ to $-7/3$. Only mean gradients are likely to govern $F_{u\theta_v}(k_x)$ when the measured ISR scaling exponents are near $-9/3$, and only dissipation quantities are likely to govern $F_{u\theta_v}(k_x)$ when the measured ISR scaling exponents are near $-5/3$.

2.7 | The decorrelation time-scale

To emphasize the interplay between the scaling exponents of $E_{ww}(k_x)$, $F_{u\theta_v}(k_x)$, and $F_{wu}(k_x)$ at different scales, $\tau(k_x)$ is also analyzed here. From the proposed formulation in Equation (18), the time-scale can be expressed as

$$\tau(k_x) = \begin{cases} -\dfrac{AF_{wu}(k_x)}{\Gamma(z)E_{ww}(k_x)}, & \text{neutral,} \\ -\dfrac{AF_{wu}(k_x)}{\Gamma(z)E_{ww}(k_x)-\beta_o F_{u\theta_v}(k_x)}, & \text{diabatic.} \end{cases} \tag{21}$$

The terms in Equation (21) can all be measured from a standard sonic anemometer. For the ISR, the scaling laws for $\tau(k_x)$ can be quite different depending on the role atmospheric stability plays. In near-neutral conditions, $F_{wu}(k_x)$ scales as $k_x^{-7/3}$ (Saddoughi & Veeravalli, 1994) whereas $E_{ww}(k_x)$ scales as $k_x^{-5/3}$. This combination recovers $\tau(k_x) \sim k_x^{-2/3}$ in the ISR. For diabatic flows where $F_{u\theta_v}(k_x)$ is significant, no unique power law may emerge. In fact, when $F_{u\theta_v}(k_x)$ becomes dominant and scales as $k_x^{-7/3}$ and upon assuming $F_{wu}(k_x)$ also scales as $k_x^{-7/3}$, $\tau(k_x)$ becomes a constant (i.e., k_x^0). Clearly, scaling laws of estimated $\tau(k_x)$ may fingerprint the dominant processes in the CSB model. Likewise, in neutral conditions and when $F_{wu}(k_x)$ scales as k_x^0, as shown by DNS (Pope, 2000) and some laboratory experiments (Saddoughi & Veeravalli, 1994), and $E_{ww}(k_x)$ experiences an energy flat region (i.e., $\sim k_x^0$), then $\tau(k_x) \sim k_x^0$ as well. Two analytical expressions for $\tau(k_x)$ are now considered:

$$\tau(k_x) = \epsilon^{-1/3}k_x^{-2/3} \quad \forall k_x \tag{22}$$

and

$$\tau_{\text{new}}(k_x) = \begin{cases} \epsilon^{-1/3}k_a^{-2/3}, & k_x \le k_a, \\ \epsilon^{-1/3}k_x^{-2/3}, & k_x > k_a, \end{cases} \tag{23}$$

in which k_a is a stability-dependent threshold to be determined. Equation (22) reflects the ISR expected behavior of $F_{wu}(k_x)$ and $E_{ww}(k_x)$, while Equation (23) can take into account less steep slopes in the low-frequency range, associated with key "break point" or transition regions in $F_{wu}(k_x)$ and $E_{ww}(k_x)$. To estimate the transitions in $E_{ww}(k_x)$ from large scales (i.e., the flat region of constant energy) to ISR, and hence k_a, even in the absence of $k_x^{-5/3}$ in the ISR, it is useful to resort to the pre-multiplied spectral representation. The pre-multiplied spectral representation is convenient for this purpose because the spectral peaks occur at frequencies that match the integral time-scale, I_s (Kaimal & Finnigan, 1994). For the definition and evaluation of I_s and the corresponding wavenumber, k_s, the reader is referred to the Appendix.

3 | DATA PRESENTATION AND METHODOLOGY

3.1 | Site characteristics

The data used were collected at the ATTO site in Brazil (Andreae *et al.*, 2015; Dias *et al.*, 2023; Dias-Júnior *et al.*, 2019; Mortarini *et al.*, 2022). The site includes two micrometeorological towers: the ATTO tower (02°08′45″S, 59°00′20″W), which is 325 m high, and the "INSTANT" tower (02°08′39″S, 59°00′00″W), which is 81 m high. The goal of these two towers is to investigate the ASL, the transition from the RSL to the ASL, and the RSL with high vertical resolution. The measurements were conducted above a tall and dense forested canopy having mean h =37 m and leaf-area index varying from 5.5–7.5 $m^2 \cdot m^{-2}$ (Chamecki *et al.*, 2020; Siqueira & Katul, 2010).

3.2 | The data

Only data collected at the INSTANT tower during the months of March, April, May, and June 2023 were used.

The three velocity components and virtual temperature were measured at multiple heights ($z/h = 0.95$, 1.16, 1.35, 1.89, and 2.19) using sonic Thies Ultrasonic Anemometer 3Ds and Galltec Mella thermohygrometers shown in Figure 1. The sampling frequency was set to f_s =10 Hz and the averaging period was 1 hour. For each one-hour run, a quality-control analysis similar to that published elsewhere (Zahn *et al.*, 2016) was applied to the velocity components u, v, and w and the sonic temperature θ_v. After the wind velocity components were rotated into the streamwise system when applying the double rotation technique (McMillen, 1988), the relevant turbulence statistics and the different conventional stability classes were evaluated as described elsewhere (Cava *et al.*, 2022; Dupont & Patton, 2012a). A summary of the number of one-hour runs at each z/h and stability regime is presented in Table 2.

TABLE 2 Number of runs for each stability class and measurement height.

z/h	Number of runs: Forced convection	Weakly stable	Very stable
0.95	13	349	164
1.16	12	324	130
1.35	13	317	111
1.89	8	241	85
2.19	12	207	76

Whether to use ζ_{sb} or ζ to classify thermal stratification remains to be clarified before presenting the CSB results. To do so, Figure 2 explores the dependence of ζ_{sb} on ζ, where ζ_{sb} is determined using Equation (4). Both quantities were evaluated at $0.95z/h$, close to the canopy top. Departing from neutral stratification in $|\zeta|$, the $|\zeta_{sb}|$ values grow, but not linearly. In the following, we purposely adopt ζ to describe the degree of stratification, for consistency with prior literature, noting that $|\zeta_{sb}|$ and ζ are correlated.

In a canonical near-neutral atmospheric boundary layer, it is common to assume that the measurements at $z/h = 0.95$ and 1.16 are associated with the RSL (Raupach & Thom, 1981), whereas the measurements at $z/h = 1.89$ and 2.19 are associated with the ASL for a typical daytime boundary-layer depth δ exceeding 1000 m (Raupach, 1981). The measurement at $z/h = 1.35$ may be deemed to be in the transitional sublayer between the RSL and ASL, as shown in Figure 1. However, for unstable and very stable stability, this classification breaks down as schematized in Figure 1. For unstable conditions, the outer layer and RSL can erode the inertial sublayer (Dias-Júnior *et al.*, 2019), whereas, for very stable conditions, the inertial subrange and the RSL are also eroded by low-frequency eddies penetrating into the canopy volume (Cava *et al.*, 2022).

3.3 | Spectra, co-spectra, and TKE dissipation calculations

When computing spectra from time series, Taylor's frozen turbulence hypothesis was used (Taylor, 1938; Wyngaard & Clifford, 1977). The application of Taylor's hypothesis in the RSL is discussed in the Appendix. All spectra and co-spectra are computed using the Welch periodogram method with a Hamming window approach. To facilitate comparisons between data and the CSB model, the spectral and co-spectral functions are presented separately for each z/h, but ensemble-averaged by stability class using ζ. These stability classes include forced convection

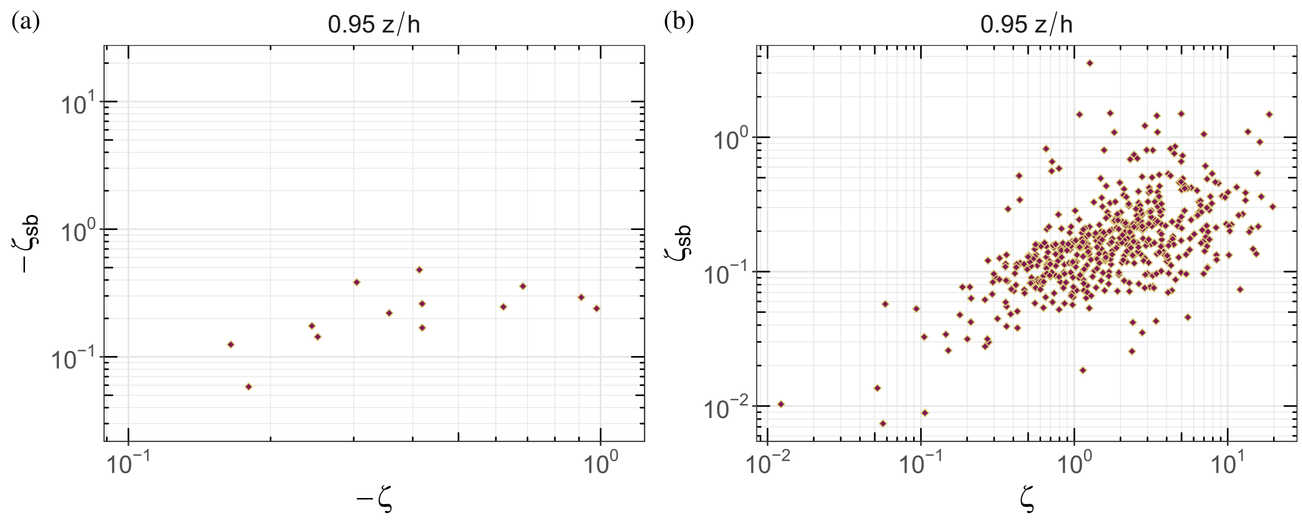

FIGURE 2 Scatter plot of ζ_{sb} against ζ in (a) forced convection and (b) weak and very stable stratification at $0.95z/h$. [Colour figure can be viewed at wileyonlinelibrary.com]

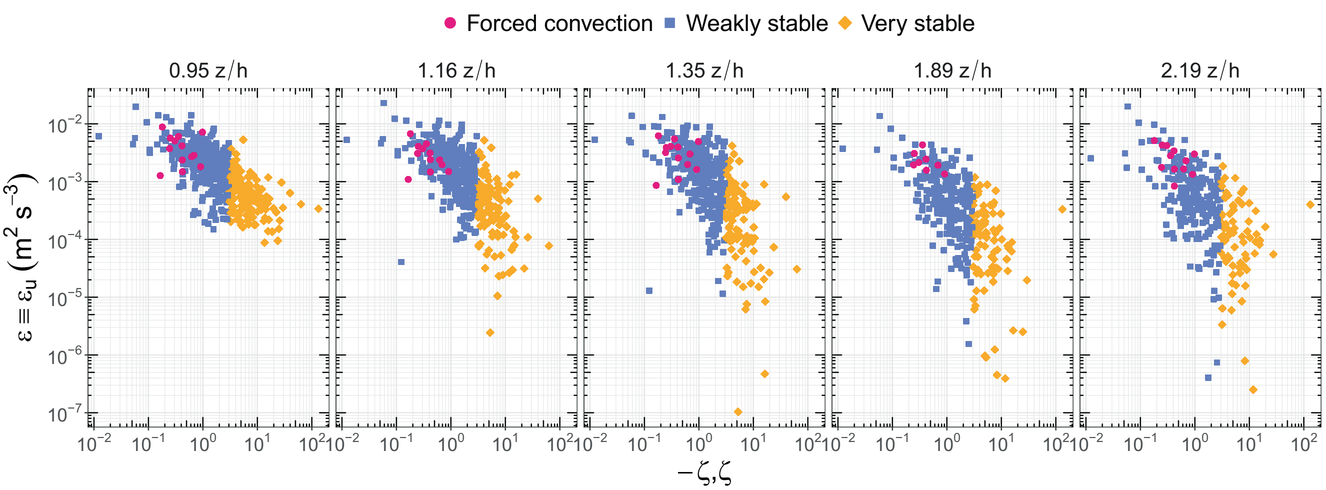

FIGURE 3 Inferred dissipation rate of turbulent kinetic energy ϵ from the longitudinal velocity spectra versus $-\zeta$ (forced convection) and ζ (stable stratification) at different z/h (shown as columns): forced convection (circles), weakly stable (squares), and very stable (diamonds) stratification. [Colour figure can be viewed at wileyonlinelibrary.com]

($-2.28 \leq \zeta < -0.10$), weakly stable ($0.1 \geq \zeta < 3$), and very stable ($\zeta \geq 3$) conditions, so as to focus on the end-member cases featured in Figure 1. The near-neutral cases have been analyzed and presented elsewhere (Mortarini *et al.*, 2023) and are not repeated here. The dissipation of turbulent kinetic energy, ϵ, was estimated from the ISR of the longitudinal velocity spectrum $E_{uu}(k_x)$. As such, these ϵ calculations are independent of $E_{ww}(k_x)$, which is a key source term to be used in the modeled $F_{uw}(k_x)$. In these calculations, a five-minute shifting window in which the spectral exponent is close to $-5/3$ in $E_{uu}(k_x)$ is used to evaluate $\epsilon_u \equiv \epsilon$ for each run. This estimate of ϵ and $\tau(k_x)$ does not require the existence of a $k_x^{-5/3}$ scaling in $E_{ww}(k_x)$. Figure 3 shows the calculated dissipation of the TKE at each height and across all stability regimes encountered.

4 | RESULTS AND DISCUSSION

To address the study objectives, the measured $F_{wu}(k_x)$ is compared with the one predicted from the CSB approach when using measured Γ, $F_{u\theta_v}(k_x)$, $E_{ww}(k_x)$, and modeled $\pi_{\text{neutral}}(k_x)$ and π_{diabatic} at all heights and stability classes. $\tau(k)$, which is the only quantity not directly measured, is estimated from Equations (22) and (23) using ϵ inferred from $E_{uu}(k_x)$ shown in Figure 3. The first subsection presents the two key spectral and co-spectral functions needed for diagnosing scalewise contributions to $F_{wu}(k_x)$ from Equation (18). The mechanical production contribution requires $E_{ww}(k_x)$ and the buoyancy contribution requires $F_{u\theta_v}(k_x)$. In the second subsection, the integral scales of $E_{ww}(k_x)$ are identified for each z/h and stability class. These integral scales are needed to assess what governs the transitions from large scales to the ISR in $F_{wu}(k_x)$. The third subsection compares measured $F_{wu}(k_x)$ with CSB modeled $F_{wu}(k_x)$ when forcing the model with measured $E_{ww}(k_x)$, $\Gamma(z)$, and $F_{u\theta_v}(k_x)$. Predictions from $\pi_{\text{neutral}}(k_x)$ and $\pi_{\text{diabatic}}(k_x)$ are then compared to assess the effects of thermal stratification on $F_{wu}(k_x)$. The last subsection carries out another diagnostic by computing the decorrelation time-scale from measured $F_{wu}(k_x)$, $E_{ww}(k_x)$, $F_{u\theta_v}(k_x)$, and $\Gamma(z)$ and comparing the outcomes with expectations in terms of scaling laws across all k_x values.

4.1 | The vertical velocity spectra and longitudinal heat-flux co-spectra

Figure 4 presents the computed median ensemble-averaged normalized $E_{ww}(k_x)$ and $F_{u\theta_v}(k_x)$ for each z/h and stability class. For $E_{ww}(k_x)$, a flat region of constant energy with $E_{ww}(k_x) \sim k_x^0$ persists at $z/h = 0.95$, 1.16, and 1.35, with minor distortions from atmospheric stability. However, at higher levels (i.e., $z/h = 1.89$ and 2.19) deemed outside the RSL and conventionally treated in the ASL, the deviations from k_x^0 are significant, especially in weakly

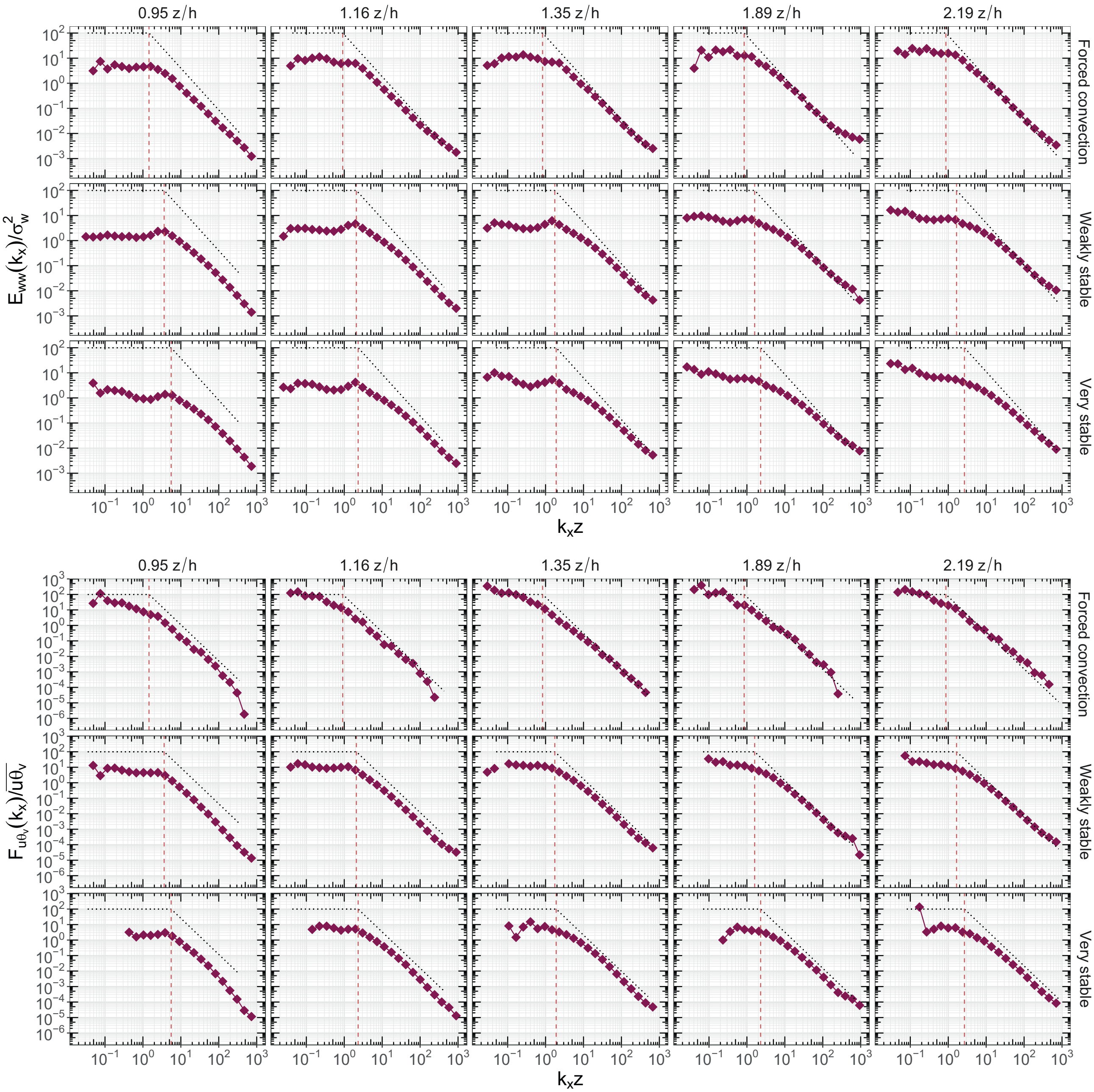

FIGURE 4 Median ensemble-averaged normalized $E_{ww}(k_x)$ and $F_{u\theta_v}(k_x)$ for each z/h and stability class. The vertical dashed line indicates k_a as identified in Section 4.2. The pointed lines represent the flat region (k_x^0) for $k_x \leq k_a$ and the ISR scaling for $k_x > k_a$. [Colour figure can be viewed at wileyonlinelibrary.com]

stable and very stable conditions. With regards to ISR scales in $E_{ww}(k_x)$, deviations from $k_x^{-5/3}$ (also shown in the figures) are also visible for all heights except $z/h = 0.95$ (in the ensemble). In fact, for weakly stable and very stable conditions, the ensemble $E_{ww}(k_x)$ exhibits an extended k_x^{-1} scaling for $z/h = 1.89$ and 2.19. In general, a k_x^{-1} scaling is associated with dimensional analysis (Kader & Yaglom, 1991) that is suggestive that z, often an inner-layer variable, is no longer relevant for $k_x z < 1$. Surprisingly, the ensemble $F_{u\theta_v}(k_x)$ is much better behaved in the ISR for all stability regimes, with slopes that are consistent with $k_x^{-7/3}$ or k_x^{-2} for both the RSL and ASL.

Because the ensemble-averaged $E_{ww}(k_x)$ deviates appreciably from expectations (i.e., $k_x^{-5/3}$ in the ISR and k_x^0 at large scales), the relative impacts of $E_{ww}(k_x)$ and $F_{u\theta_v}(k_x)$ on $F_{wu}(k_x)$ can thus be assessed by comparing measured scaling exponents characterizing $F_{wu}(k_x)$ at all heights, stability classes, and range of scales with those of $F_{u\theta_v}(k_x)$ and $\tau(k_x)E_{ww}(k_x)$. To facilitate identification of the transition regions associated with k_a in $F_{wu}(k_x)$, $E_{ww}(k_x)$ is considered. This choice has already been discussed in the theory section and is motivated by the findings here that $E_{ww}(k_x)$ seems to be most sensitive to thermal stratification at various z/h, at least when compared with $F_{u\theta_v}(k_x)$.

4.2 | Integral scales and transition regimes

To identify the transition wavenumber k_a, the pre-multiplied $k_x E_{ww}(k_x)$ spectra are first computed for all z/h and stability classes. Two estimates are featured. The first uses the Kaimal spectrum (Equation A4). Assuming $\beta = 5/3$, the a_1 and a_2 parameters of the spectrum are determined using nonlinear regression fitting to the ensemble-averaged $fE_{ww}(f)$ and I_s is computed from the optimized a_1 and converted to k_s using Taylor's frozen turbulence hypothesis. The second estimate, only used in stable stratification, finds the maximum in $k_x E_{ww}(k_x)$ numerically and then identifies the corresponding k_x associated with this maximum.

The transition wavenumber evaluated from the pre-multiplied vertical velocity spectra in each run as the median estimate of k_a is shown in Figure 5. The box

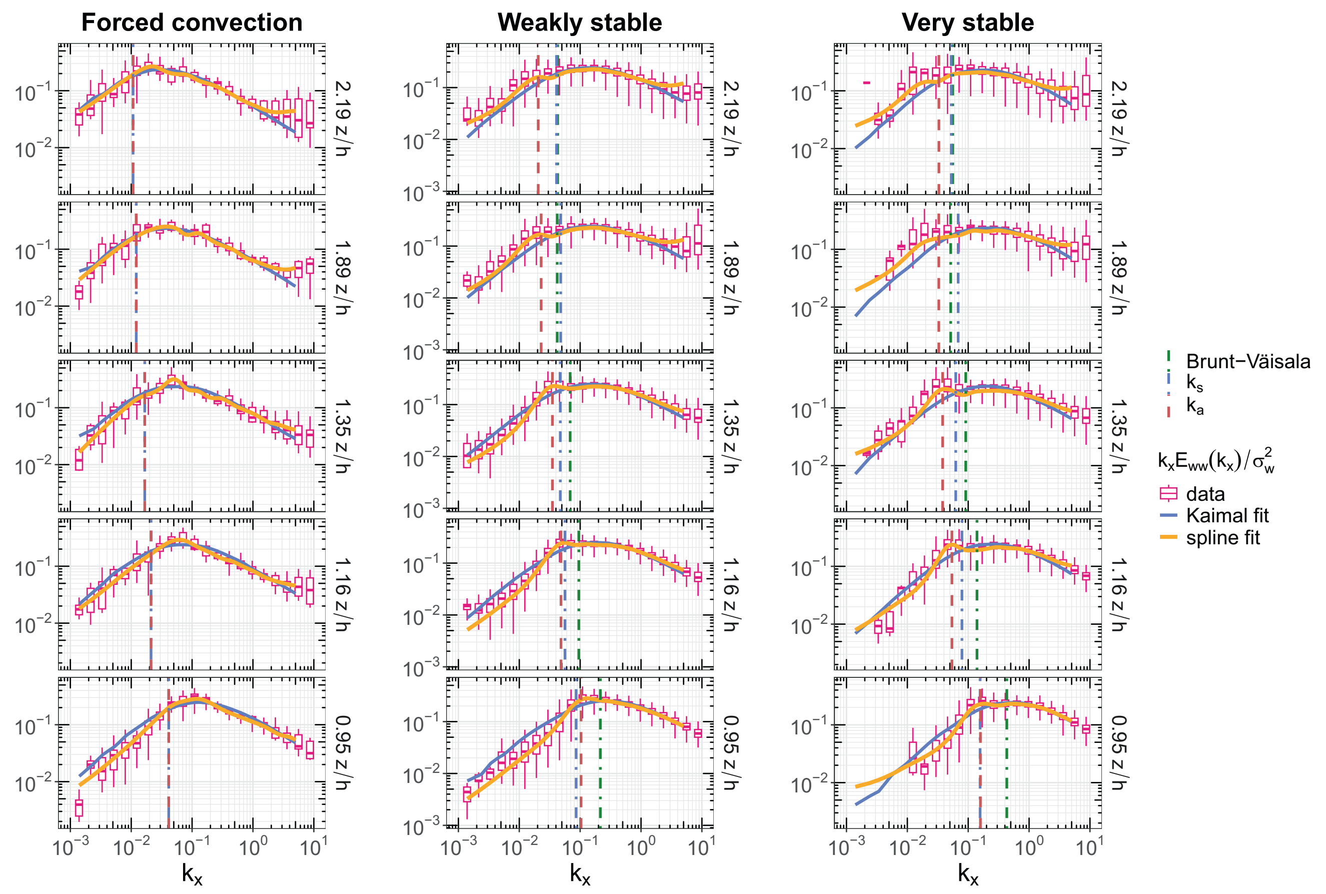

FIGURE 5 Box plot of the pre-multiplied vertical velocity spectrum $k_x E_{ww}(k_x)$ as a function of k_x. The Kaimal spectrum (blue, Equation A4) and the spline fit (yellow) to the ensemble-averaged pre-multiplied spectra are shown. The vertical lines represent the peaks associated with the median of k_a, k_s, and the wavenumber associated with the BV frequency. [Colour figure can be viewed at wileyonlinelibrary.com]

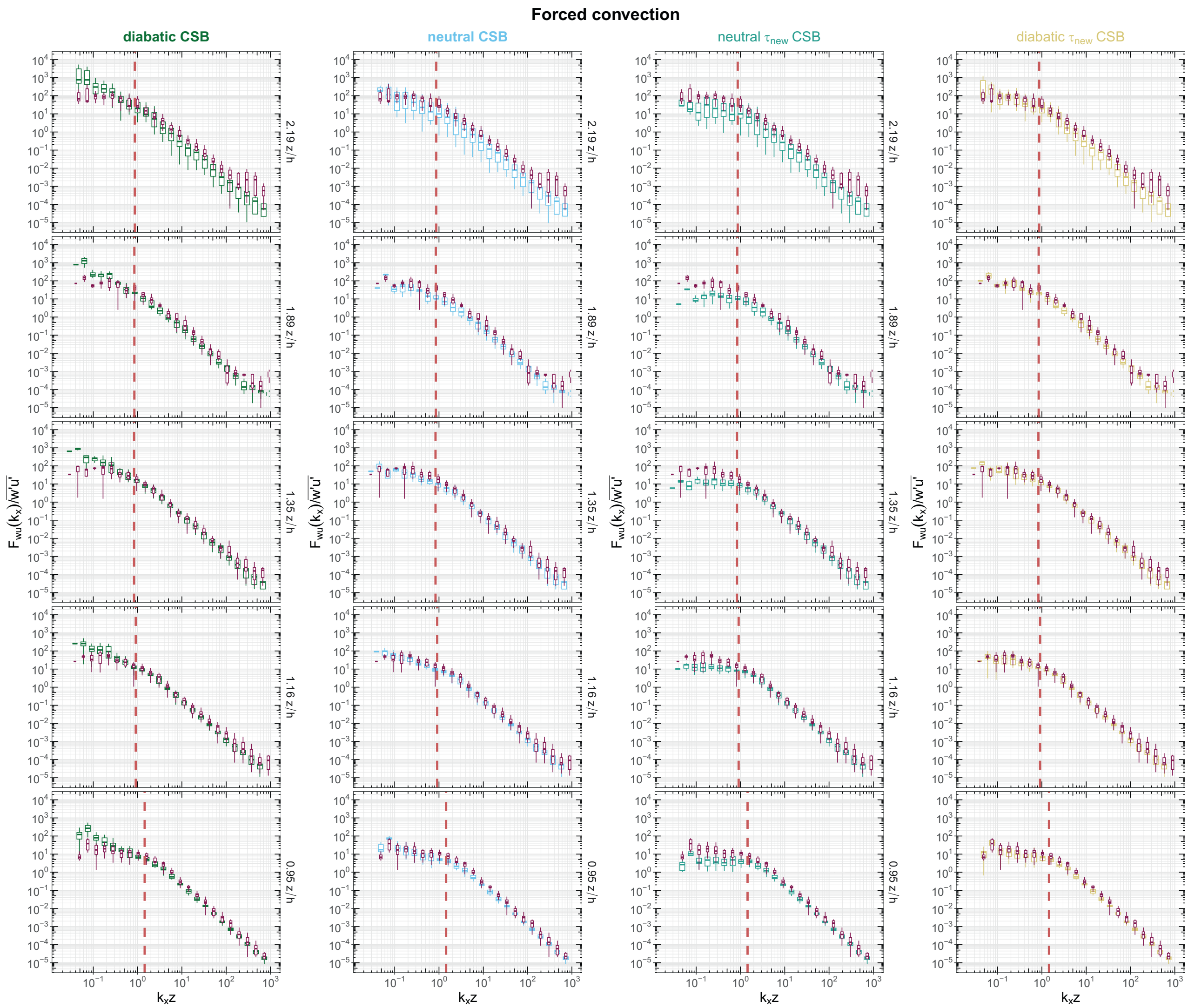

FIGURE 6 Comparison between measured (purple) and modeled normalized $F_{wu}(k_x)$ as a function of normalized wavenumber for all z/h in forced convection. The peak in the pre-multiplied vertical spectrum associated with k_a is also shown (vertical dashed line). [Colour figure can be viewed at wileyonlinelibrary.com]

plots of the individual $k_x E_{ww}(k_x)$ are compared with the ensemble average of a spline fit (yellow line) and a fit based on Equation A4 (blue line). In forced convection, the spline fit shows good agreement with the Kaimal function for all z/h, suggesting that the integral scale evaluated with Equation (A4) is a robust estimate for k_a, the median value of which shifts to lower frequencies as z/h increases. Hence, in forced convection $k_a \equiv k_s$. Reflecting the behavior of the box plots of the individual spectra in weak and very stable stratification, the spline fits of the pre-multiplied median average spectra exhibit two maxima: one in the ISR and one at lower frequency. In stable conditions, the internal wave frequencies at any z/h must be less than the Brunt–Väisälä (BV) frequency, given by $N_{BV} = \sqrt{\beta_o \Gamma_\theta}$. This frequency can be converted to an equivalent wavelength using Taylor's frozen turbulence hypothesis. Superimposing this wavelength (green dash–dotted line) on the pre-multiplied spectra in Figure 5 suggests that the large deviations from the peaks determined by the Kaimal spectra can be partly explained by the limits set by the BV frequency. Interestingly, close to the canopy top, k_s is smaller than the wavenumber associated with the BR frequency; as z/h increases, the two tend to coincide, while a secondary peak at low k_x emerges. In stable stratification, the transition wavenumber is identified as the secondary maximum of the pre-multiplied vertical velocity spectrum at wavenumbers less than the wavenumber associated with BV.

The analysis here demonstrates that, for stable conditions in the ASL, the vertical velocity spectra are distorted appreciably by thermal stratification and their peaks are not linked to z but to the BV frequency. The consequence of such distortion on $F_{wu}(k_x)$ is now considered.

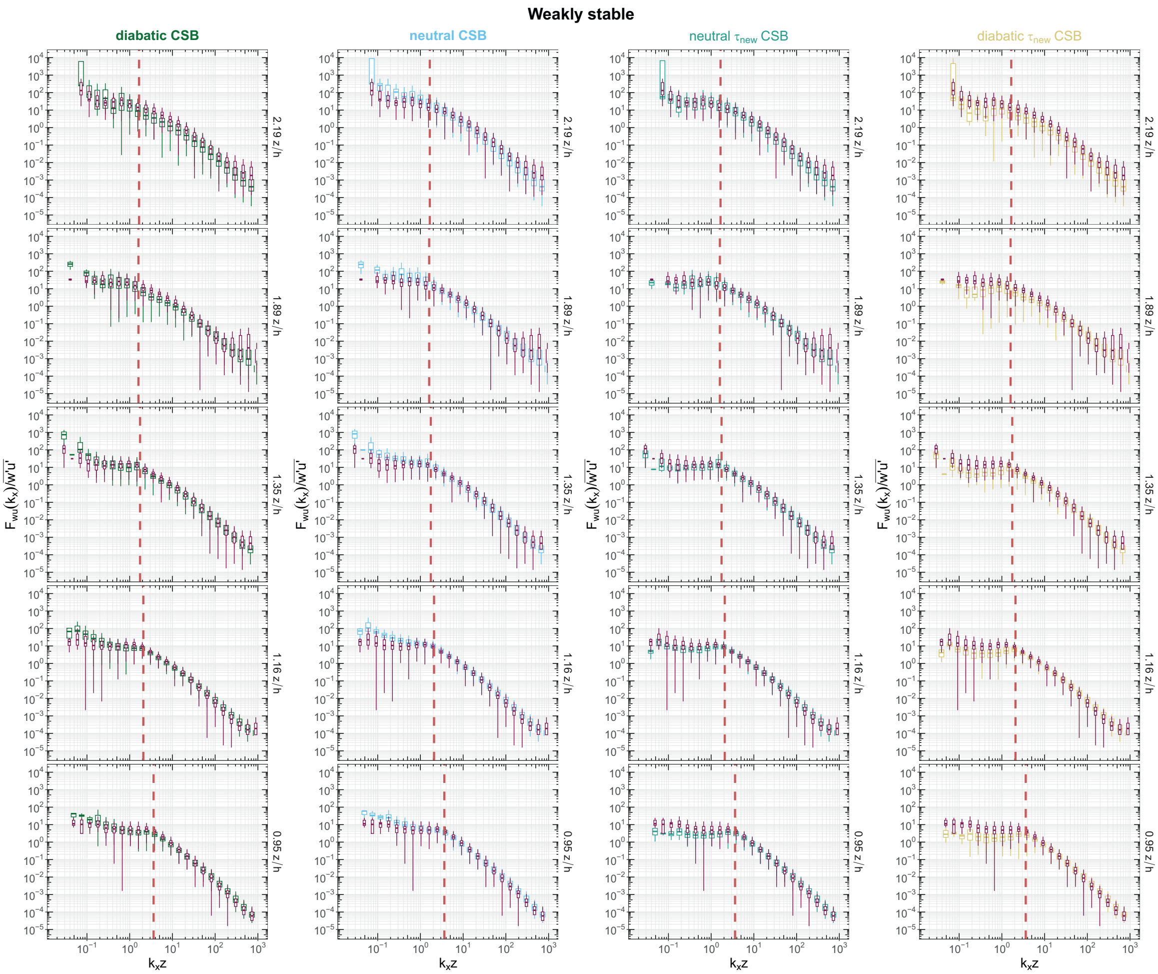

FIGURE 7 Comparison between measured (purple) and modeled normalized $F_{wu}(k_x)$ as a function of normalized wavenumber for all z/h in weakly stable stratification. The peak in the pre-multiplied vertical spectrum associated with k_a is also shown (vertical dashed line). [Colour figure can be viewed at wileyonlinelibrary.com]

4.3 | Diagnostic evaluation of the CSB model

Using the measured $E_{ww}(k_x)$, the measured $\Gamma(z)$, the measured $F_{u\theta_v}(k_x)$, and the modeled $\tau(k_x)$ and $\tau_{new}(k_x)$, Equation (18) is used to predict $F_{wu}(k_x)$ and those predictions are then compared with the measured co-spectrum shown in Figures 6–8 for forced convection, weakly stable stratification, and very stable stratification. Box plots of $F_{wu}(k_x)$ evaluated from data are compared with the following variants of the CSB model:

- the computed $F_{wu}(k_x)$ using τ defined by Equation (22) and $\pi_{neutral}(k_x)$, with no contributions from $F_{u\theta_v}(k_x)$;
- the computed $F_{wu}(k_x)$ using τ_{new} defined by Equation (23) and $\pi_{neutral}(k_x)$, with no contributions from $F_{u\theta_v}(k_x)$;
- the computed $F_{wu}(k_x)$ using τ defined by Equation (22) and $\pi_{diabatic}(k_x)$;
- the computed $F_{wu}(k_x)$ using τ_{new} defined by Equation (23) and $\pi_{diabatic}(k_x)$.

For each stability class and height above the canopy, a red dashed vertical line marks the transition wavenumber k_a. For $k_x > k_a$, all model variants perform well, indicating that the $F_{u\theta_v}(k_x)$ contribution to the co-spectral budget is negligible in the ISR.

In forced convection, for $k_x \leq k_a$, the combination of $\pi_{diabatic}(k_x)$ and τ_{new} provides the best agreement across all z/h. However, near the tree crowns, the difference between the neutral model with τ and the diabatic model with τ_{new} is minimal. Under weakly stable stratification, for $k_x \leq k_a$, the neutral CSB model using $\tau(k_x)$ slightly overestimates the lowest wavenumbers, whereas the diabatic CSB model with $\tau(k_x)$, as well as the models incorporating $\tau_{new}(k_x)$, captures the low-frequency behavior better. This suggests that, under weakly stable conditions, it is challenging to assess whether the shape of the momentum co-spectrum is governed primarily by the

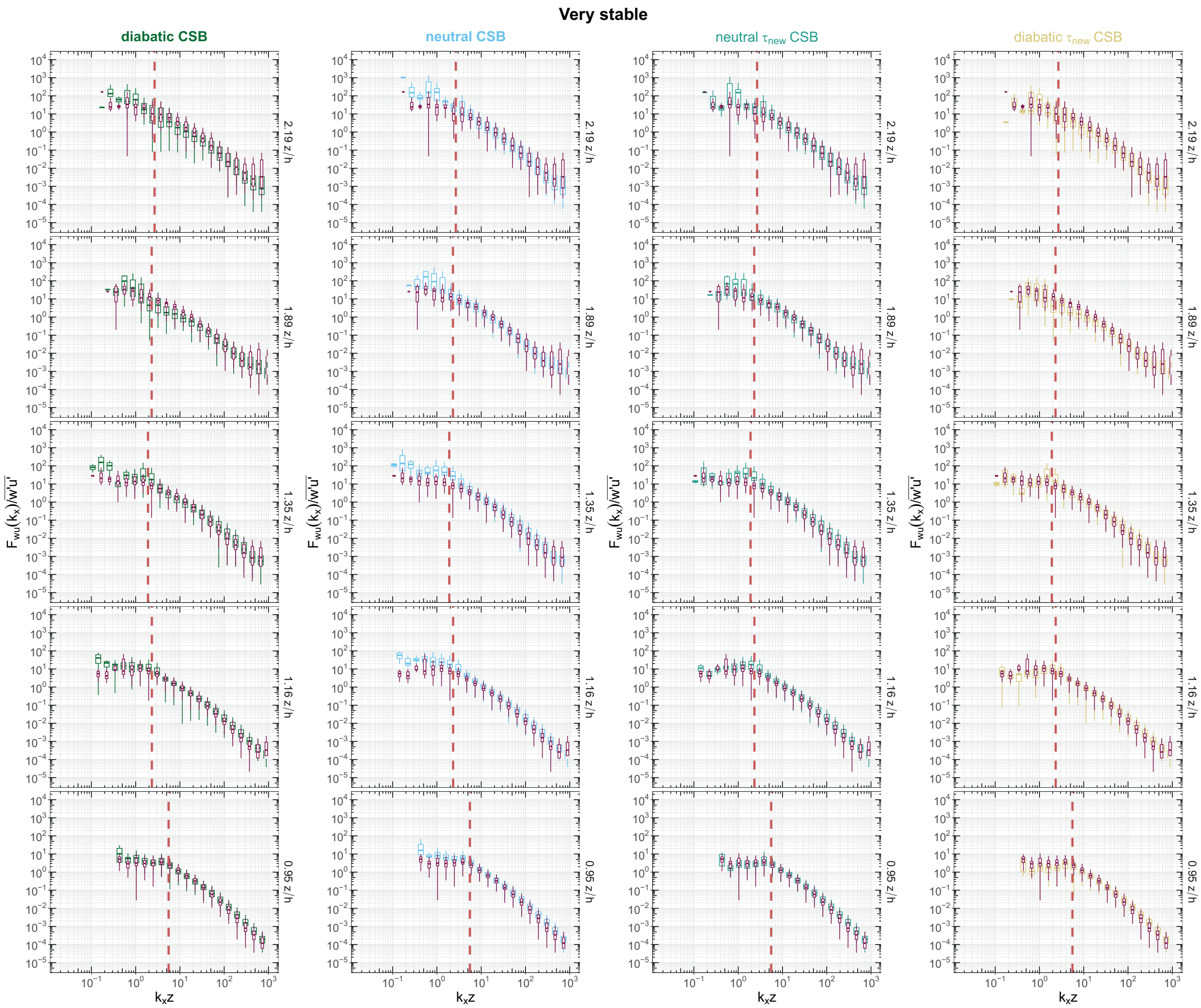

FIGURE 8 Comparison between measured (purple) and modeled normalized $F_{wu}(k_x)$ as a function of normalized wavenumber for all z/h in very stable stratification. The peak in the pre-multiplied vertical spectrum associated with k_a is also shown (vertical dashed line). [Colour figure can be viewed at wileyonlinelibrary.com]

vertical spectrum through $\tau_{new}(k_x)$ or by the horizontal heat flux. In very stable stratification, CSB variations with $\tau(k_x)$ also overestimate $F_{wu}(k_x)$ from the data. Unlike in weakly stable conditions, the diabatic CSB with τ_{new} performs better, suggesting that low-frequency contributions to the momentum budget, arising from submeso phenomena and gravity waves, are effectively accounted for by the horizontal heat-flux co-spectrum.

4.4 | Scaling relations for the decorrelation time-scale

An alternative approach to the comparisons between measured versus modeled $F_{wu}(k_x)$ is to compute $\tau(k_x)$ using Equation (21) and compare it with expectations from the ISR scaling analysis. Here, all the necessary quantities for computing $\tau(k_x)$ from Equation (21) are actually supplied by the measurements. The computed $\tau(k_x)$, in its diabatic (yellow) and neutral (green) formulations, is shown in Figure 9 across all z/h and stability classes. To emphasize deviations in scaling laws from expectations in the ISR, the decorrelation time is normalized by $\epsilon^{-1/3}k_x^{-2/3}$. If $\tau(k_x)$ satisfied Equation (22), then the expected behavior would be a flat line, while if it satisfied Equation (23) then the expected behavior would be a flat line for $k_x > k_a$ and a line with a 2/3 slope for $k_x \leq k_a$.

Overall, both the diabatic and the neutral representations confirm that $\tau(k_x)$ (i) is roughly constant for wavenumbers smaller than k_a (as proposed in Equation 23) and (ii) scales as $\epsilon^{-1/3}k_x^{-2/3}$ for the ISR regime below $1.35z/h$. The diabatic formulation does not result in constant $\tau(k_x)$ values in the ISR in both weak and very stable stratification, especially at the higher level. At wavenumbers ($k_x z > 100$), noise contamination increases $\tau(k_x)$, causing large deviations from the expected ISR scaling. This noise does not contribute significantly to $\overline{w'u'}$

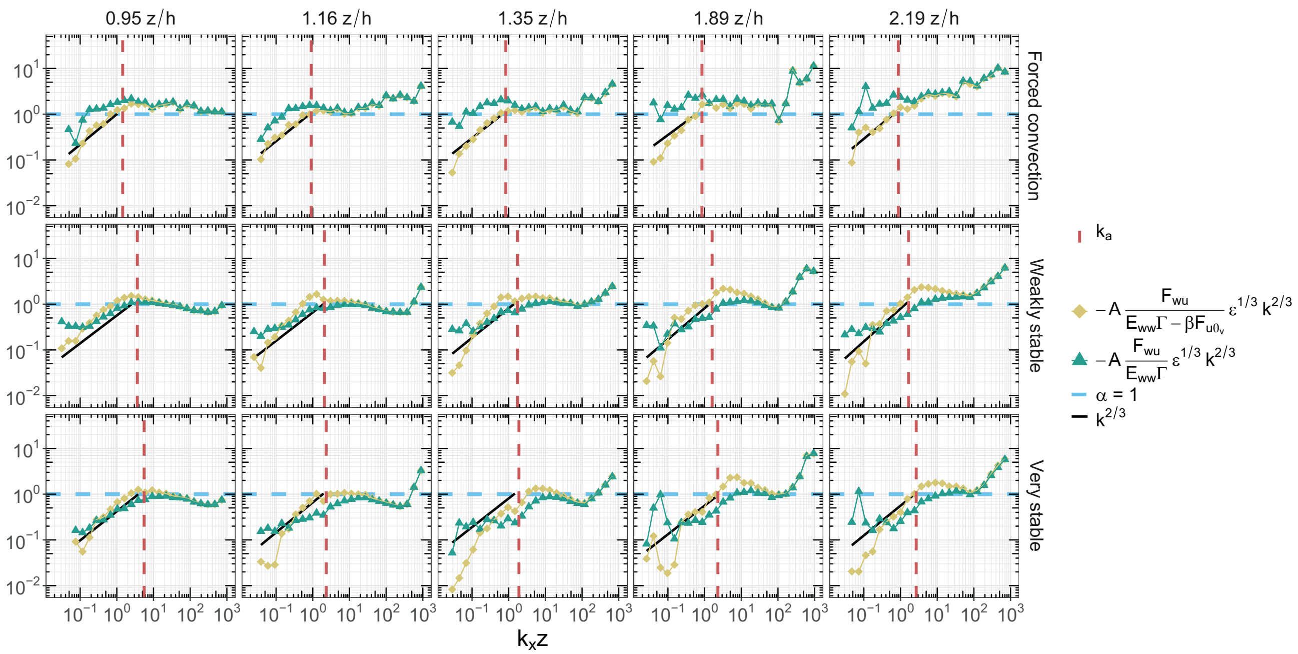

FIGURE 9 Calculation of the normalized decorrelation time $\tau(k_x)$ as a function of wavenumber k_x using Equation (21). A horizontal line at unity indicates $\tau(k_x) = \alpha\epsilon^{1/3}k_x^{2/3}$ with $\alpha = 1$, while a black line identifies $\tau(k_x) = \text{const} = \epsilon^{1/3}k_a^{2/3}$. [Colour figure can be viewed at wileyonlinelibrary.com]

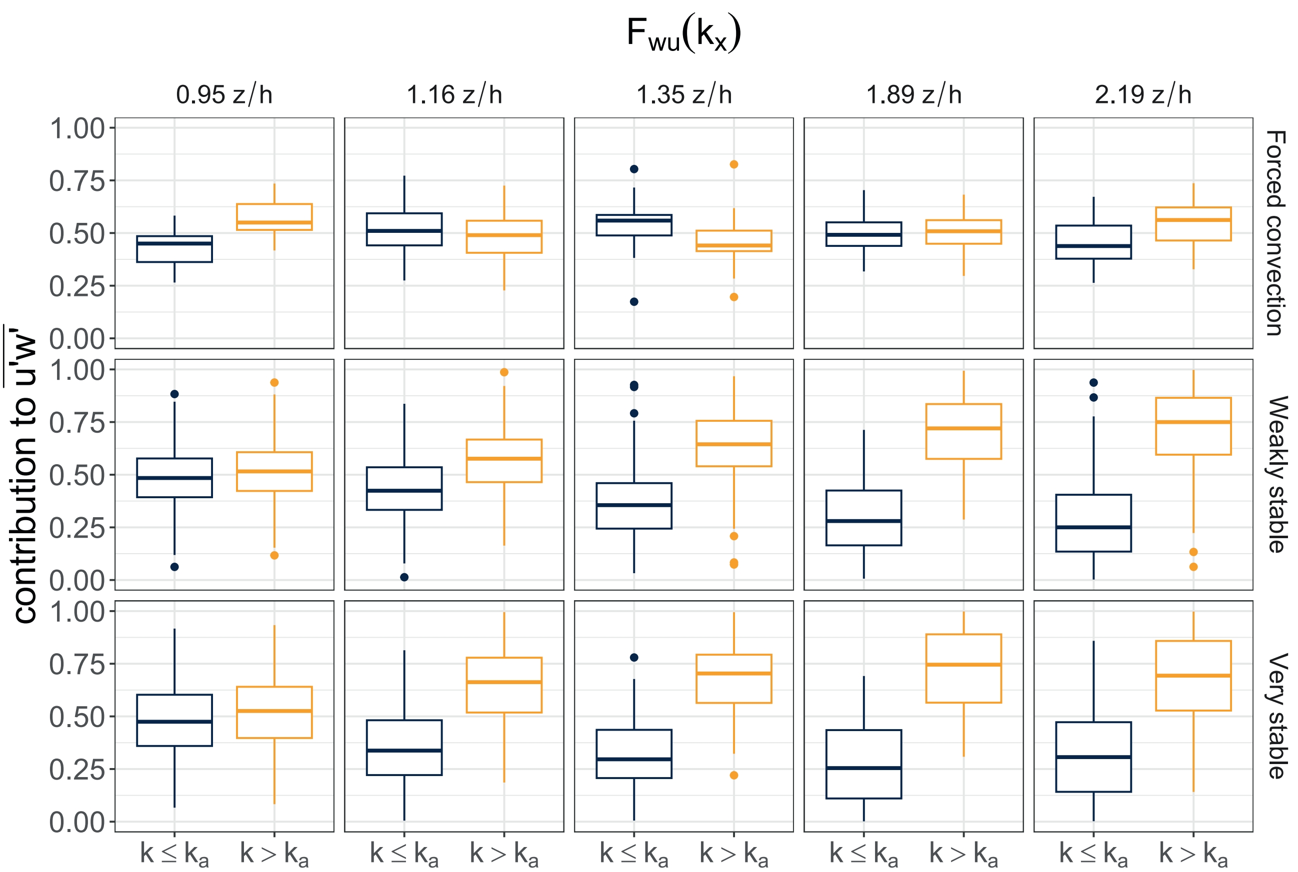

FIGURE 10 Contribution to the turbulent momentum flux, $\overline{w'u'}$, of the large scales, $k \leq k_a$, and the inertial scales, $k > k_a$, for each stability class and measurement height. [Colour figure can be viewed at wileyonlinelibrary.com]

despite the large $\tau(k_x)$ determined here. Interestingly, the coefficient $\alpha = 1$ approximates the best-fitting $\tau(k_x)$ better at all z/h and stability classes compared with other coefficients derived in the near-neutral RSL (Mortarini *et al.*, 2023). Recall that $\alpha = 1$ results in C_{uw} predictions that are in agreement with empirical values reported in the literature, as noted earlier.

The scalewise approach of the CSB enables the identification of each scale's contribution to the overall turbulent momentum flux. Both the CSB model and the decorrelation time-scale comparison confirm that, while the expected scaling laws hold in the ISR, the scaling of $F_{wu}(k_x)$, $E_{ww}(k_x)$ becomes less evident at low wavenumbers. This raises the question of how much each range contributes to the total momentum flux. Figure 10 illustrates the contributions of large scales $k_x \le k_a$ and inertial scales $k_x > k_a$ to $\overline{w'u'}$. In forced convection, both ranges contribute equally, whereas in weakly and stably stratified conditions wavenumbers beyond the transition become the dominant contributors to the scalewise integral of $F_{wu}(k_x)$, with their influence increasing with increasing z/h. Thus, inertial subrange eddies, often labelled as "detached" eddies in wall bounded flows, contribute significantly to momentum transfer in the RSL and ASL for diabatic conditions. The fact that the canopy is a porous medium means it does not suppress turbulence as much as solid boundaries do in canonical boundary layers, enabling ISL eddies to move momentum efficiently.

5 | CONCLUSIONS

The work here sought to assess the scalewise impact of thermal stratification on the turbulent momentum flux in the RSL and ASL above a tall canopy. The newly proposed co-spectral budget model linked the co-spectrum of the momentum flux to the energy spectrum of the vertical velocity through a scalewise mechanical production term and the co-spectrum of the longitudinal heat flux through a scalewise buoyancy production (or destruction) term. The energy spectrum of the vertical velocity and the co-spectrum of the longitudinal heat flux were supplied externally using data collected in the RSL and ASL and across different atmospheric stability regimes. These stability regimes were also communicated indirectly through their effects on the measured mean velocity gradient and the inferred turbulent kinetic energy dissipation rate needed for representing the decorrelation time. The outcomes from this work revealed the following.

1. In the ISR, the vertical velocity energy spectrum was much more impacted by thermal stratification compared with the longitudinal heat-flux co-spectrum. For the ASL and for stable and very stable conditions, large departures from the expected $k_x^{-5/3}$ scaling were observed in the inertial subrange of the vertical velocity. Exponents that appear closer to k_x^{-1} approximate the vertical velocity spectral measurements better even at small scales.
2. The scalewise decorrelation time between u' and w' was approximated by two regimes: $\epsilon^{-1/3}k_a^{-2/3}$ at large scales and $\epsilon^{-1/3}k_x^{-2/3}$ at inertial subrange scales. The transition wavenumber k_a between these two regimes was related to the integral scale of the vertical velocity fluctuations. This integral scale appears to be described reasonably by the Brunt–Väisälä frequency for the ASL and for stable stratification.
3. A co-spectral budget model that accounts for the aforementioned scalewise decorrelation time, measured mean longitudinal velocity gradient, measured vertical velocity energy spectrum, and measured longitudinal heat-flux co-spectrum describes the measured co-spectrum between u' and w' at all instrument-resolved wavenumbers. This diagnostic model also shows that any attempts to predict momentum transport from the energetics of the flow (i.e., vertical velocity spectra) must include the horizontal heat-flux co-spectrum. The interplay between only these budget terms is somewhat encouraging, given the terrain non-uniformity and land-cover heterogeneity associated with the ATTO site.
4. The longitudinal heat-flux co-spectrum showed an approximate $k_x^{-7/3}$ scaling within the inertial subrange and a near-constant regime (i.e., k_x^0) for the RSL and ASL and all stability classes. Moving from the RSL to the ASL, the spectral transition region from k_x^0 to $k_x^{-7/3}$ broadens across scales and is not well described by a single "break point".
5. The analysis also suggests that, for the turbulent stress budget, the appropriate length-scale to use for stability characterization need not be the Obukhov length. The latter was developed from considerations of the turbulent kinetic energy budget, not the turbulent stress budget. Thus, future stability correction functions to momentum transport may include both the Obukhov length and L_{sb}, which is derived from Equation (4). While stability measures based on L_{sb} and ζ are correlated, they are not identical.

The work here calls for further experiments, analysis, theories, and simulations for the longitudinal heat-flux co-spectrum in the RSL, as it may be the dominant term in momentum transport at large scales. This buoyancy term is much less studied compared with its sensible heat-flux counterpart, but may be more significant for turbulent stresses and momentum fluxes.

ACKNOWLEDGEMENTS

The authors thank the Instituto Nacional de Pesquisas da Amazônia (INPA), the Max-Planck Society, the German Federal Ministry of Education and Research (BMBF Contract Nos. 01LB1001A, 01LK1602A, and 01LK1602B), the Brazilian Ministério da Ciência, Tecnologia e Inovação (MCTI/FINEP Contract No. 01.11.01248.00), the Amazon State University (UEA), FAPEAM, CAPES and SDS/CEUC/RDS-Uatumã for their financial support. We also thank the LBA Micrometeorology Lab, especially Leonardo R. de Oliveira and Jailson da Mata, for their assistance in maintaining the equipment and processing the raw data at the ATTO site.

This project was supported in part by an appointment to the NRC Research Associateship Program at Air Resources Laboratory, National Oceanic and Atmospheric Administration, administered by the Fellowships Office of the National Academies of Sciences, Engineering, and Medicine.

C. Q. Dias-Júnior acknowledges support from CNPq (307530/2022-1; 406884-2022-6).

G. Katul acknowledges support from the US National Science Foundation (NSF-AGS-2028633) and the Department of Energy (DE-SC0022072). I. Mammarella acknowledges support from ICOS-FI via University of Helsinki funding and the EU Horizon Europe Framework Programme for Research and Innovation (GreenFeedback no. 101056921). Open access publishing facilitated by Universita degli Studi di Milano, as part of the Wiley - CRUI-CARE agreement.

DATA AVAILABILITY STATEMENT

The data that support the findings of this study are available from the corresponding author upon reasonable request.

ORCID

Luca Mortarini https://orcid.org/0000-0002-0543-2975
Cléo Quaresma Dias-Júnior https://orcid.org/0000-0003-4783-4689

REFERENCES

Andreae, M.O., Acevedo, O.C., Araùjo, A., Artaxo, P., Barbosa, C.G.G., Barbosa, H.M.J. et al. (2015) The Amazon tall tower observatory (ATTO): overview of pilot measurements on ecosystem ecology, meteorology, trace gases, and aerosols. *Atmospheric Chemistry and Physics*, 15(18), 10723–10776.

Antonia, R. & Zhu, Y. (1994) Inertial range behaviour of the longitudinal heat flux cospectrum. *Boundary-Layer Meteorology*, 70, 429–434.

Ayet, A., Katul, G., Bragg, A. & Redelsperger, J.L. (2020) Scale-wise return to isotropy in stratified boundary layer flows. *Journal of Geophysical Research: Atmospheres*, 125(16), e2020JD032732.

Besnard, D., Harlow, F., Rauenzahn, R. & Zemach, C. (1996) Spectral transport model for turbulence. *Theoretical and Computational Fluid Dynamics*, 8(1), 1–35.

Bos, W.J.T., Touil, H., Shao, L. & Bertogli, J. (2004) On the behavior of the velocity-scalar cross correlation spectrum in the inertial range. *Physics of Fluids*, 16, 3818–3823.

Brunet, Y. (2020) Turbulent flow in plant canopies: historical perspective and overview. *Boundary-Layer Meteorology*, 177(2), 315–364.

Brunet, Y. & Irvine, M.R. (2000) The control of coherent eddies in vegetation canopies: Streamwise structure spacing, canopy shear scale and atmospheric stability. *Boundary-Layer Meteorology*, 94(1), 139–163.

Brutsaert, W. (1982) *Evaporation into the atmosphere: theory, history and applications*, vol. 1. Dordrecht: Springer Science & Business Media.

Caughey, S., Wyngaard, J. & Kaimal, J. (1979) Turbulence in the evolving stable boundary layer. *Journal of Atmospheric Sciences*, 36(6), 1041–1052.

Cava, D. & Katul, G. (2012) On the scaling laws of the velocity-scalar cospectra in the canopy sublayer above tall forests. *Boundary-Layer Meteorology*, 145, 351–367.

Cava, D., Katul, G., Scrimieri, A., Poggi, D., Cescatti, A. & Giostra, U. (2006) Buoyancy and the sensible heat flux budget within dense canopies. *Boundary-Layer Meteorology*, 118, 217–240.

Cava, D., Dias-Júnior, C.Q., Acevedo, O., Oliveira, P.E.S., Tsokankunku, A., Sörgel, M. et al. (2022) Vertical propagation of submeso and coherent structure in a tall and dense Amazon Forest in different stability conditions PART I: flow structure within and above the roughness sublayer. *Agricultural and Forest Meteorology*, 322, 108983.

Chamecki, M., Freire, L.S., Dias, N.L., Chen, B., Dias-Junior, C.Q., Toledo Machado, L.A. et al. (2020) Effects of vegetation and topography on the boundary layer structure above the Amazon forest. *Journal of the Atmospheric Sciences*, 77(8), 2941–2957.

Charuchittipan, D. & Wilson, J. (2009) Turbulent kinetic energy dissipation in the surface layer. *Boundary-Layer Meteorology*, 132(2), 193–204.

Choi, K.S. & Lumley, J.L. (2001) The return to isotropy of homogeneous turbulence. *Journal of Fluid Mechanics*, 436, 59–84.

Chowdhuri, S., Ghannam, K. & Banerjee, T. (2022) A scale-wise analysis of intermittent momentum transport in dense canopy flows. *Journal of Fluid Mechanics*, 942, A51.

Corrêa, P.B., Dias-Júnior, C.Q., Cava, D., Sörgel, M., Botía, S., Acevedo, O. et al. (2021) A case study of a gravity wave induced by Amazon forest orography and low level jet generation. *Agricultural and Forest Meteorology*, 307, 108457.

Corrsin, S. (1975) Limitations of gradient transport models in random walks and in turbulence. In: Frenkiel, F.N. & Munn, R.E. (Eds.) *Advances in geophysics*, vol. 18. Virginia: Elsevier, pp. 25–60.

Deshpande, R., de Silva, C.M. & Marusic, I. (2023) Evidence that superstructures comprise self-similar coherent motions in high Reynolds number boundary layers. *Journal of Fluid Mechanics*, 969, A10.

Dias, N.L., Toro, I.M.C., Dias-Júnior, C.Q., Mortarini, L. & Brondani, D. (2023) The relaxed eddy accumulation method over the Amazon forest: the importance of flux strength on individual and aggregated flux estimates. *Boundary-Layer Meteorology*, 189(1), 139–161. Available from: https://doi.org/10.1007/s10546-023-00829-7

Dias-Júnior, C.Q., Dias, N.L., dos Santos, R.M.N., Sörgel, M., Araújo, A., Tsokankunku, A. et al. (2019) Is there a classical inertial sublayer over the Amazon forest? *Geophysical Research Letters*, 46(10), 5614–5622.

Dupont, S. & Patton, E.G. (2012a) Influence of stability and seasonal canopy changes on micrometeorology within and above an orchard canopy: the CHATS experiment. *Agricultural and Forest Meteorology*, 157, 11–29.

Dupont, S. & Patton, E.G. (2012b) Momentum and scalar transport within a vegetation canopy following atmospheric stability and seasonal canopy changes: the CHATS experiment. *Atmospheric Chemistry and Physics*, 12(13), 5913–5935.

Durbin, P. (1993) A Reynolds stress model for near-wall turbulence. *Journal of Fluid Mechanics*, 249, 465–498.

Everard, K., Katul, G., Lawrence, G., Christen, A. & Parlange, M. (2021) Sweeping effects modify Taylor's frozen turbulence hypothesis for scalars in the roughness sublayer. *Geophysical Research Letters*, 48(22), e2021GL093746.

Finnigan, J.J., Shaw, R.H. & Patton, E.G. (2009) Turbulence structure above a vegetation canopy. *Journal of Fluid Mechanics*, 637, 387–424.

Garratt, J. (1992) *The atmospheric boundary layer*. Cambridge, Great Britain: Cambridge University Press.

Hanjalić, K. & Launder, B. (2021) Reassessment of modeling turbulence via Reynolds averaging: a review of second-moment transport strategy. *Physics of Fluids*, 33(9), 091302.

Harman, I.N. & Finnigan, J.J. (2007) A simple unified theory for flow in the canopy and roughness sublayer. *Boundary-Layer Meteorology*, 123(2), 339–363.

Harman, I.N. & Finnigan, J.J. (2008) Scalar concentration profiles in the canopy and roughness sublayer. *Boundary-Layer Meteorology*, 129(3), 323–351.

He, G., Jin, G. & Yang, Y. (2017) Space-time correlations and dynamic coupling in turbulent flows. *Annual Review of Fluid Mechanics*, 49(1), 51–70.

Hsieh, C.I. & Katul, G.G. (1997) Dissipation methods, Taylor's hypothesis, and stability correction functions in the atmospheric surface layer. *Journal of Geophysical Research: Atmospheres*, 102(D14), 16391–16405.

Kader, B. & Yaglom, A. (1990) Mean fields and fluctuation moments in unstably stratified turbulent boundary layers. *Journal of Fluid Mechanics*, 212, 637–662.

Kader, B. & Yaglom, A. (1991) Spectra and correlation functions of surface layer atmospheric turbulence in unstable thermal stratification. In: *Turbulence and Coherent Structures*. Dordrecht: Springer, pp. 387–412.

Kaimal, J. (1973) Turbulenece spectra, length scales and structure parameters in the stable surface layer. *Boundary-Layer Meteorology*, 4, 289–309.

Kaimal, J.C. & Finnigan, J.J. (1994) *Atmospheric boundary layer flows: their structure and measurement*. New York: Oxford University Press.

Kaimal, J.C., Wyngaard, J., Izumi, Y. & Coté, O. (1972) Spectral characteristics of surface-layer turbulence. *Quarterly Journal of the Royal Meteorological Society*, 98(417), 563–589.

Katul, G. & Albertson, J.D. (1998) An investigation of higher-order closure models for a forested canopy. *Boundary-Layer Meteorology*, 89, 47–74.

Katul, G.G. & Albertson, J.D. (1999) Modeling CO2 sources, sinks, and fluxes within a forest canopy. *Journal of Geophysical Research: Atmospheres*, 104(D6), 6081–6091.

Katul, G., Konings, A. & Porporato, A. (2011) Mean velocity profile in a sheared and thermally stratified atmospheric boundary layer. *Physical Review Letters*, 107(26), 268502.

Katul, G.G., Porporato, A., Manes, C. & Meneveau, C. (2013a) Co-spectrum and mean velocity in turbulent boundary layers. *Physics of Fluids*, 25(9), 091702.

Katul, G.G., Li, D., Chamecki, M. & Bou-Zeid, E. (2013b) Mean scalar concentration profile in a sheared and thermally stratified atmospheric surface layer. *Physical Review E*, 87(2), 023004.

Katul, G.G., Porporato, A., Shah, S. & Bou-Zeid, E. (2014) Two phenomenological constants explain similarity laws in stably stratified turbulence. *Physical Review E*, 89(2), 023007.

Kolmogorov, A.N. (1941) Dissipation of energy under locally isotropic turbulence. *Dokl Akad Naukl SSSR*, 32, 16–18.

Launder, B., Reece, G. & Rodi, W. (1975) Progress in the development of a Reynolds-stress turbulence closure. *Journal of Fluid Mechanics*, 68, 537–566.

Li, D. (2019) Turbulent Prandtl number in the atmospheric boundary layer-where are we now? *Atmospheric Research*, 216, 86–105.

Li, D. & Katul, G.G. (2017) On the linkage between the $k^{-5/3}$ spectral and $k^{-7/3}$ cospectral scaling in high-Reynolds number turbulent boundary layers. *Physics of Fluids*, 29(6), 065108.

Li, D., Katul, G.G. & Zilitinkevich, S.S. (2016) Closure schemes for stably stratified atmospheric flows without turbulence cutoff. *Journal of the Atmospheric Sciences*, 73(12), 4817–4832.

Lumley, J. (1965) Interpretation of time spectra measured in high-intensity shear flows. *Physics of Fluids*, 8(6), 1056–1062.

Lumley, J.L. (1967) Similarity and the turbulent energy spectrum. *Physics of Fluids*, 10, 855–858.

McMillen, R.T. (1988) An eddy correlation technique with extended applicability to non-simple terrain. *Boundary-Layer Meteorology*, 43(3), 231–245.

Mendonça, A.C.S., Dias-Júnior, C.Q., Acevedo, O.C., Marra, D.M., Cely-Toro, I.M., Fisch, G. et al. (2025) Estimation of the nocturnal boundary layer height over the Central Amazon forest using turbulence measurements. *Agricultural and Forest Meteorology*, 367, 110469.

Monin, A.S. & Obukhov, A.M. (1954) Basic laws of turbulent mixing in the surface layer of the atmosphere. *Contrib Geophys Inst Acad Sci USSR*, 151(163), e187.

Mortarini, L., Dias-Júnior, C.Q., Acevedo, O., Oliveira, P.E.S., Tsokankunku, A., Sörgel, M. et al. (2022) Vertical propagation of submeso and coherent structure in a tall and dense amazon forest in different stability conditions. PART II: coherent structures analysis. *Agricultural and Forest Meteorology*, 322, 108993.

Mortarini, L., Katul, G.G., Cava, D., Dias-Junior, C.Q., Dias, N.L., Manzi, A. et al. (2023) Adjustments to the law of the wall above

an Amazon forest explained by a spectral link. *Physics of Fluids*, 35(2), 025102.
Poggi, D., Katul, G. & Albertson, J. (2004a) Momentum transfer and turbulent kinetic energy budgets within a dense model canopy. *Boundary-Layer Meteorology*, 111(3), 589–614.
Poggi, D., Porporato, A., Ridolfi, L., Albertson, J. & Katul, G. (2004b) The effect of vegetation density on canopy sub-layer turbulence. *Boundary-Layer Meteorology*, 111(3), 565–587.
Pope, S.B. (2000) *Turbulent flows*. Cambridge, UK: Cambridge University Press.
Raupach, M.R. (1981) Conditional statistics of Reynolds stress in rough-wall and smooth-wall turbulent boundary layers. *Journal of Fluid Mechanics*, 108, 363–382.
Raupach, M. & Thom, A. (1981) Turbulence in and above plant canopies. *Annual Review of Fluid Mechanics*, 13(1), 97–129.
Raupach, M.R., Finnigan, J.J. & Brunet, Y. (1996) Coherent eddies and turbulence in vegetation canopies: the mixing-layer analogy. *Boundary-Layer Meteorology*, 78, 351–382.
Saddoughi, S. & Veeravalli, S. (1994) Local isotropy in turbulent boundary layers at high Reynolds number flow. *Journal of Fluid Mechanics*, 268, 333–372.
Shaw, R.H., Brunet, Y., Finnigan, J.J. & Raupach, M.R. (1995) A wind tunnel study of air flow in waving wheat: two-point velocity statistics. *Boundary-Layer Meteorology*, 76(4), 349–376.
Siqueira, M. & Katul, G. (2002) Estimating heat sources and fluxes in thermally stratified canopy flows using higher-order closure models. *Boundary-Layer Meteorology*, 103, 125–142.
Siqueira, M.B. & Katul, G.G. (2010) An analytical model for the distribution of CO2 sources and sinks, fluxes, and mean concentration within the roughness sub-layer. *Boundary-Layer Meteorology*, 135(1), 31–50.
Siqueira, M., Lai, C.T. & Katul, G. (2000) Estimating scalar sources, sinks, and fluxes in a forest canopy using Lagrangian, Eulerian, and hybrid inverse models. *Journal of Geophysical Research: Atmospheres*, 105(D24), 29475–29488.
Taylor, G.I. (1938) The spectrum of turbulence. *Proceedings of the Royal Society of London. Series A: Mathematical and Physical Sciences*, 164(919), 476–490.
Tennekes, H. & Lumley, J.L. (1972) *A first course in turbulence*. Cambridge, MA: MIT Press.
Thomas, C., Mayer, J.C., Meixner, F.X. & Foken, T. (2006) Analysis of low-frequency turbulence above tall vegetation using a Doppler sodar. *Boundary-Layer Meteorology*, 119(3), 563–587.
van de Wiel, B.J.H., Moene, A.F., Steeneveld, G.J., Hartogensis, O.K. & Holtslag, A.A.M. (2007) Predicting the collapse of turbulence in stably stratified boundary layers. *Flow, Turbulence and Combustion*, 79(3), 251–274.
de Wiel, B.J.H.V., Moene, A.F., Jonker, H.J.J., Baas, P., Basu, S., Donda, J.M.M. et al. (2012a) The minimum wind speed for sustainable turbulence in the nocturnal boundary layer. *Journal of the Atmospheric Sciences*, 69(11), 3116–3127.
de Wiel, B.J.H.V., Moene, A.F. & Jonker, H.J.J. (2012b) The cessation of continuous turbulence as precursor of the very stable nocturnal boundary layer. *Journal of the Atmospheric Sciences*, 69(11), 3097–3115.
Wilson, N.R. & Shaw, R.H. (1977) A higher order closure model for canopy flow. *Journal of Applied Meteorology and Climatology*, 16, 1197–1205.
Wyngaard, J.C. (2010) *Turbulence in the atmosphere*. Cambridge, UK: Cambridge University Press.
Wyngaard, J. & Clifford, S. (1977) Taylor's hypothesis and high–frequency turbulence spectra. *Journal of Atmospheric Sciences*, 34(6), 922–929.
Wyngaard, J. & Coté, O. (1972) Cospectral similarity in the atmospheric surface layer. *Quarterly Journal of the Royal Meteorological Society*, 98(417), 590–603.
Zahn, E., Chor, L. & Dias, N.L. (2016) A simple methodology for quality control of micrometeorological datasets. *American Journal of Environmental Engineering*, 6(4A), 135–142.

How to cite this article: Mortarini, L., Katul, G., Mauricio Cely-Toro, I., Quaresma Dias-Júnior, C. & Mammarella, I. (2025) The role of thermal stratification on the co-spectral properties of momentum transport above an Amazonian forest. *Quarterly Journal of the Royal Meteorological Society*, e5024. Available from: https://doi.org/10.1002/qj.5024

APPENDIX A. INTEGRAL TIME-SCALE EVALUATION

The definition of the integral time-scale I_s of a zero mean and unit variance flow variable s' is given as

$$I_s = \int_0^\infty \rho_{ss}(\tau)\, d\tau, \tag{A1}$$

where τ is the time lag and $\rho_{ss}(\tau) = \overline{s'(t)s'(t+\tau)}$ is the auto-correlation function of s'. The integral time-scale is used routinely as a measure of the memory or decorrelation time (Tennekes & Lumley, 1972). For the zero mean $\bar{s} = 0$ and unit variance ($\sigma_s^2 = 1$) stochastic process s, the energy spectrum $E_{ss}(f)$ is the Fourier transform of the auto-correlation function $\rho_{ss}(\tau)$ and is given by

$$E_{ss}(f) = \frac{1}{2\pi}\int_{-\infty}^{\infty} \rho_{ss}(\tau)\exp(-if\tau)\, d\tau, \tag{A2}$$

where $i^2 = -1$ and f is the frequency. It follows directly that

$$E_{ss}(0) = \frac{1}{2\pi}\int_{-\infty}^{\infty} \rho_{ss}(\tau)\, d\tau = \frac{I_s}{\pi}, \tag{A3}$$

when using $\rho_{ss}(-\tau) = \rho_{ss}(\tau)$. Spectral analysis of finite time series cannot estimate $E_{ss}(0)$, as this estimate requires an infinite sampling duration. A pre-multiplied spectrum with a preset mathematical form, hereafter referred to as the Kaimal spectrum (Kaimal & Finnigan, 1994), is used and is given as

$$fE_{ss}(f) = \frac{a_1 f}{(1+a_2 f)^\beta}. \tag{A4}$$

This pre-multiplied form has a maximum or peak at frequency $f_p = [a_2(\beta - 1)]^{-1}$, as can be shown by differentiating the premultiplied spectrum with respect to f, setting the outcome to zero, and solving for f_p, the frequency at which the pre-multiplied spectrum peaks. Moreover, the variance $\sigma_s^2 = 1$ can be derived by integrating $E_{ss}(f)$ over all f to give an expression for a_1:

$$\sigma_s^2 = 1 = \int_0^\infty E_{ss}(f)\, df = \frac{a_1}{a_2(\beta - 1)} = a_1 f_p. \tag{A5}$$

Noting that the actual (not the pre-multiplied) spectrum can be evaluated at $f = 0$, the following outcomes emerge:

$$E_{ss}(0) = a_1 = \frac{\sigma_{ss}^2}{f_p} = \frac{1}{f_p} = \frac{I_s}{\pi}. \tag{A6}$$

That is, the integral time-scale of a flow variable can be readily determined from f_p using $I_s = \pi / f_p$ provided $\beta > 1$ (Kaimal & Finnigan, 1994). For $\beta = 1$, the variance is unbounded. Hereafter, the integral time-scale for any flow variable s' is indicated by I_s and can be converted to a wavenumber, k_s, using Taylor's frozen turbulence hypothesis.

APPENDIX B. TAYLOR'S HYPOTHESIS

The use of Taylor's hypothesis in the roughness sublayer (RSL) is supported by both experimental evidence and theoretical considerations. Recent wind-tunnel experiments compared velocity spectra (longitudinal and vertical) obtained by means of a particle imaging velocimeter (PIV) and cross probe at very high Reynolds numbers. The PIV velocity spectra (space–time) did not utilize Taylor's hypothesis, whereas the cross-probe measurements in time did. The agreement between the two spectra along k_x was exceptionally high for scales up to 6δ (Deshpande *et al.*, 2023). In the ISR, a number of corrections to Taylor's hypothesis have been derived. These corrections do not alter k_x, but lead to adjustments of the Kolmogorov constants with squared turbulent intensity (Hsieh & Katul, 1997; Lumley, 1965; Wyngaard & Clifford, 1977). A more realistic adjustment to Taylor's hypothesis that accommodates random sweeping effects has been proposed and is known as the elliptic approximation (He *et al.*, 2017). This approximation assumes that finer eddies may be swept randomly by the energetics of larger eddies, much like the mean flow advects turbulence. The elliptic approximation was investigated experimentally using an array of temperature sensors within the RSL of a vineyard (Everard *et al.*, 2021). These experiments have shown that the advection velocity of eddies remains commensurate with the mean streamwise velocity $\overline{U}$. However, the squared sweeping velocity responsible for the elliptic shape of the space–time autocorrelation function appears to scale linearly with the measured turbulent kinetic energy even within the canopy volume. For these reasons, Taylor's hypothesis will be used without any modifications.